Simultaneous Photoradiochemical Labeling of Antibodies for Immuno-Positron Emission Tomography

Patra, Malay ; Klingler, Simon ; Eichenberger, Larissa S ; Holland, Jason P

Abstract: A method for the simultaneous (one-step) photochemical conjugation and 89Zr-radiolabeling of antibodies is introduced. A photoactivatable chelate based on the functionalization of desferrioxamine B with an arylazide moiety (DFO-ArN3, [1]) was synthesized. The radiolabeled complex, 89Zr-1+, was produced and characterized. Density functional theory calculations were used to investigate the mechanism of arylazide photoactivation. 89Zr-radiolabeling experiments were also used to determine the efficiency of photochemical conjugation. A standard two-step approach gave a measured conjugation efficiency of 3.5% ± 0.4%. In contrast, the one-step process gave a higher photoradiolabeling efficiency of 76%. Stability measurements, cellular saturation binding assays, positron emission tomographic imaging, and biodistribution studies in mice bearing SK-OV-3 tumors confirmed the biochemical viability and tumor specificity of photoradiolabeled [89Zr]ZrDFO-azepin-trastuzumab. Experimental data support the conclusion that the combination of photochemistry and radiochemistry is a viable strategy for producing radiolabeled proteins for imaging and therapy.

DOI: https://doi.org/10.1016/j.isci.2019.03.004

iScience

CellPress

Article

Simultaneous Photoradiochemical Labeling of Antibodies for Immuno-Positron Emission Tomography

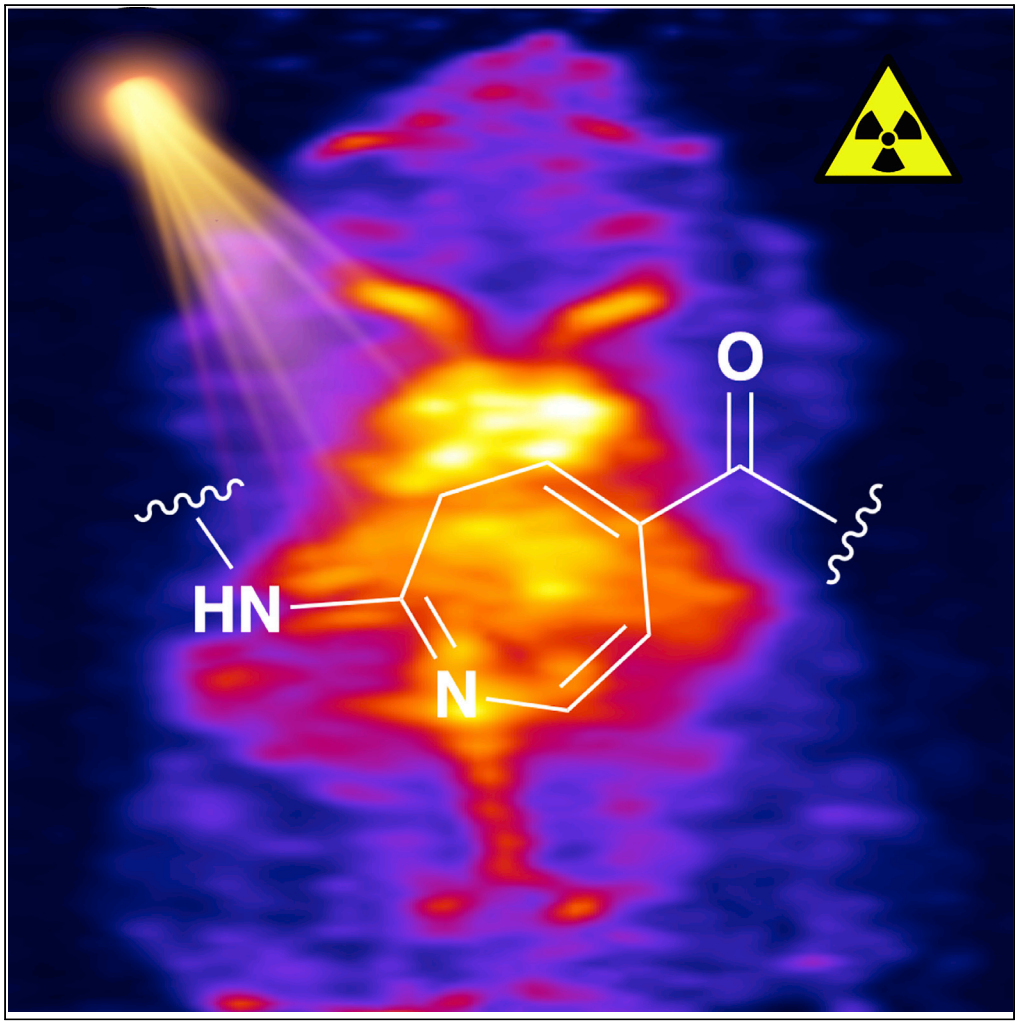

Malay Patra, Simon Klingler, Larissa S. Eichenberger, Jason P. Holland

jason.holland@chem.uzh.ch, http://www.hollandlab.org

HIGHLIGHTS

Photochemistry is combined with radiochemistry for radiosynthesis in a flash

Simultaneous *photoradiochemistry* is achieved with high radiolabeling efficiency

Photoradiochemistry produces viable ^{89}Zr-radiolabeled antibodies

Density functional theory calculations elucidate the photoactivation mechanism

Patra et al., iScience *13*, 416–431
March 29, 2019
https://doi.org/10.1016/j.isci.2019.03.004

iScience

CellPress

Article

Simultaneous Photoradiochemical Labeling of Antibodies for Immuno-Positron Emission Tomography

Malay Patra,[1,2] Simon Klingler,[1] Larissa S. Eichenberger,[1] and Jason P. Holland[1,3,*]

SUMMARY

A method for the simultaneous (one-step) photochemical conjugation and ^{89}Zr-radiolabeling of antibodies is introduced. A photoactivatable chelate based on the functionalization of desferrioxamine B with an arylazide moiety (DFO-ArN_3, [1]) was synthesized. The radiolabeled complex, ^{89}Zr-1$^+$, was produced and characterized. Density functional theory calculations were used to investigate the mechanism of arylazide photoactivation. ^{89}Zr-radiolabeling experiments were also used to determine the efficiency of photochemical conjugation. A standard two-step approach gave a measured conjugation efficiency of 3.5% ± 0.4%. In contrast, the one-step process gave a higher photoradiolabeling efficiency of ~76%. Stability measurements, cellular saturation binding assays, positron emission tomographic imaging, and biodistribution studies in mice bearing SK-OV-3 tumors confirmed the biochemical viability and tumor specificity of photoradiolabeled [^{89}Zr]ZrDFO-azepin-trastuzumab. Experimental data support the conclusion that the combination of photochemistry and radiochemistry is a viable strategy for producing radiolabeled proteins for imaging and therapy.

INTRODUCTION

The use of photochemically activated compounds for labeling proteins and other biologically active molecules was introduced by Westheimer and co-workers in 1962 (Singh et al., 1962). Since then, photoaffinity labeling (PAL) has matured, and a wide array of reagents are available for studying the structure and function of biological systems (Bayley and Knowles, 1977; Chowdhry and Westheimer, 1979; Kotzyba-Hilbert et al., 1995). Photochemical activation offers a number of advantages over thermochemical processes. For instance, photoreactive groups can be selected whereby, (1) the reagent is stable under ambient conditions, (2) photoactivation occurs specifically at a wavelength that is not absorbed by the biological vector, and (3) the conjugation step involves a chemoselective reaction with the target molecule. Furthermore, because photochemical activation proceeds via an excited electronic state that generates extremely reactive intermediates like carbenes, nitrenes, and radicals, the rates of photochemical conjugation reactions can be several orders of magnitude faster than those of standard methods (Dennler et al., 2015; Gritsan and Platz, 2006; Klán and Wirz, 2009; Platz, 1995). High reactivity of the photo-induced intermediates presents both advantages and disadvantages. One of the benefits is that photoactive reagents can yield high labeling efficiencies in short reaction times. However, to achieve efficient conjugation, PAL methods often rely on a mechanism in which the photoactive reagent and the target protein form a non-covalent pre-association complex. Pre-association facilitates pseudo-first-order intramolecular bond formation and minimizes the probability of quenching by background media (i.e., by the solvent, oxygen, salts, etc.). However, the problem with this approach is that it restricts most PAL tools to systems that self-assemble.

From the radiochemistry perspective, photochemical reactions are an attractive platform for developing radiotracers. For molecules that undergo radioactive decay, chemical kinetics is one of the main factors in determining if a reaction is suitable for use in radiotracer synthesis (Holland, 2018). As photochemical reactions often proceed with rate constants that tend toward the rate of diffusion, combining photochemistry with radiochemistry (*photoradiochemistry*) is a logical step.

Several groups have reported the use of photochemical reactions in the synthesis of radiolabeled compounds (Hashizume et al., 1995; Kumar et al., 2015; Kym et al., 1995; Lange et al., 2002; Nishikawa et al., 2003; Pandurangi et al., 1997a, 1997c; 1997b, 1998; Rajagopalan et al., 2002; Stalteri and Mather, 1996; Sykes et al., 1995, 1997; Wester et al., 1996). However, it is surprising that to date, photochemistry has had minimal impact on radiopharmaceutical science. The main bottlenecks to a more widespread use of

[1]University of Zurich, Department of Chemistry, Winterthurerstrasse 190, Zurich 8057, Switzerland

[2]Present address: Department of Chemical Sciences, Tata Institute of Fundamental Research, Homi Bhabha Road, Mumbai 400005, India

[3]Lead Contact

*Correspondence: jason.holland@chem.uzh.ch, http://www.hollandlab.org

https://doi.org/10.1016/j.isci.2019.03.004

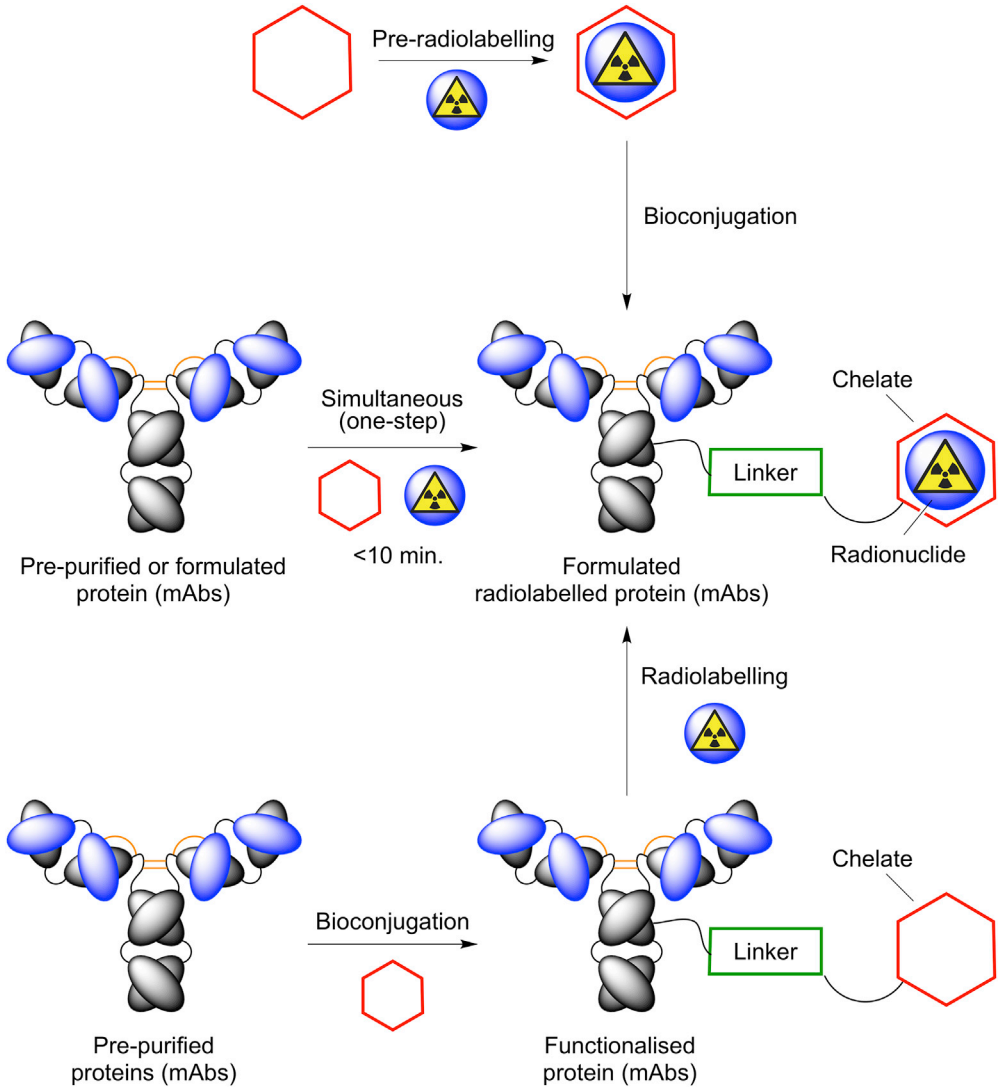

Scheme 1. Mechanistic Routes toward Radiolabeled Antibodies and Other Proteins

photoradiochemistry for labeling proteins, peptides, and small molecules are (1) avoiding the need to form a pre-associated complex, (2) controlling chemoselectivity in the presence of competing nucleophiles, and (3) ensuring that the rate of productive *bimolecular* conjugation exceeds that of background quenching reactions. If a photochemical process can be tuned to favor bimolecular coupling, then photoradiochemistry may become a more general tool in radiotracer synthesis.

A specific area for potential applications of photoradiochemistry is the synthesis of radiolabeled monoclonal antibodies (mAbs) or immunoglobulin fragments for use in positron emission tomography (immuno-PET) and radioimmunotherapy (Boros and Holland, 2018). Zirconium-89 ($t_{1/2}$ = 78.41 h) has emerged as the radionuclide of choice for immuno-PET. In almost all available methods for radiolabeling mAbs, the production of ^{89}Zr-mAbs relies on a two-step procedure (Scheme 1). Initially, the antibody is purified from a source and then functionalized with a suitable metal-ion-binding chelate. For ^{89}Zr, the chelate of choice is usually a derivative of desferrioxamine B (DFO), but a number of alternative chelates have been reported (Boros and Holland, 2018). After conjugation, the functionalized mAb is re-purified, characterized, and stored before radiolabeling. Although this two-step approach is highly successful, there are several drawbacks. First, the conjugation chemistry is time consuming and may involve multiple chemical transformations that risk compromising the biological integrity of the mAb. Second, for applications in the clinic,

the conjugation chemistry should ideally be performed in accordance with current Good Manufacturing Practice. Third, the conjugated mAb is a new molecular entity, which may be subject to stringent testing, including expensive toxicological test. Finally, storage of the radiolabeling precursor raises concerns over the long-term chemical and biochemical stability.

We postulated that photoradiochemistry could be used to streamline the production of radiolabeled mAbs (and other radiolabeled proteins or peptides) by simplifying the procedure to a one-pot reaction and eliminating the need to isolate or store the functionalized intermediate. Two mechanistically distinct processes can be envisaged for a one-pot procedure: a two-step pre-radiolabeling approach and a one-step pathway in which the radiolabeling and photochemical conjugation reactions occur simultaneously. Here, we present detailed experimental and theoretical data evaluating the photoradiochemical synthesis of ^{89}Zr-labeled trastuzumab.

RESULTS AND DISCUSSION

Our initial proof-of-concept studies found that the macrocyclic chelate, (2-(4,7-bis(carboxymethyl)-1,4,7-triazonan-1-yl)pentanedioic acid (NODAGA), when functionalized with a photoreactive arylazide (ArN_3) facilitated a two-step photoradiolabeling of trastuzumab with $^{68}Ga^{3+}$ ions (Eichenberger et al., 2019; Patra et al., 2019). Although technically feasible, the combination of short-lived ^{68}Ga ($t_{1/2}$ = 67.71 min) with mAbs (~150 kDa) is not ideal because of the mismatch between the timescales of radioactive decay and radiotracer pharmacokinetics *in vivo*. In addition, $^{68}Ga^{3+}$ radiochemistry usually requires acidic media (to avoid hydrolysis of the metal ion), which is suboptimal for photochemical conjugation using the ArN_3 group (Borden et al., 2000; Gritsan and Platz, 2010, 2006; Gritsan and Pritchina, 1992). Here, we focused our efforts on developing a photoradiochemical process for producing ^{89}Zr-labeled mAbs. Zirconium-89 radiochemistry normally starts from the zirconium tetraoxalate anion, $[^{89}Zr][Zr(C_2O_4)_4]^{4-}$(aq.), and complexation by DFO derivatives can be accomplished over a wide pH range (from approximately pH 5–10, with optimal yields attained by using pH 6–8.5) (Holland and Vasdev, 2014; Vosjan et al., 2010). Thus ^{89}Zr-radiochemistry is not only ideal for immuno-PET but also facilitates simultaneous photoradiolabeling.

Chemical and Radiochemical Synthesis

The photoactive chelate DFO-ArN_3 (**1**) was synthesized by using standard chemical transformations (Scheme 2). The compound was isolated in high purity by semi-preparative high-performance liquid chromatography and characterized by ultrahigh-performance liquid chromatography (UHPLC), high-resolution electrospray ionization mass spectrometry (HR-ESI-MS), one- and two-dimensional ^{1}H and ^{13}C nuclear magnetic resonance spectroscopies, and electronic absorption spectroscopy (Transparent Methods Figures S2–S8).

The non-radioactive complex, $[ZrDFO\text{-}ArN_3]^+$ (Zr-**1**$^+$), was prepared by the reaction of compound **1** with $ZrCl_4$(aq.), and characterized by HR-ESI-MS and UHPLC (Figure 1 and Transparent Methods Figures S9 and S10). The radiolabeled complex $[^{89}Zr][ZrDFO\text{-}ArN_3]^+$ (^{89}Zr-**1**$^+$) was prepared as a single radioactive species, the identity of which was confirmed by comparison of retention times with the authenticated non-radioactive sample and by standard co-injection methods (Figure 1, blue radiotrace).

Photochemical Kinetics

After confirming that ^{89}Zr-**1**$^+$ could be prepared via standard radiolabeling methods, the photochemical activity of compound **1** was tested under irradiation with UV light. Three separate light sources were tested including two variable-intensity light-emitting diodes (LEDs) with peak emission wavelengths at ~365 nm and ~395 nm and a high-powered Rayonet reactor (Transparent Methods Figure S1). The photochemical degradation kinetics of compound **1**, induced by using variable light intensities, was monitored by UHPLC (Figure 2 and Transparent Methods Table S2). Experiments confirmed that compound **1** was photoactive. All peaks in the UHPLC associated with photodegraded products were found to be more hydrophilic than the parent compound, which is consistent with the established mechanism of ArN_3 activation in aqueous media (Klán and Wirz, 2009). After light absorption, ArN_3 releases N_2(g) and forms a short-lived arylnitrene species in the singlet ($^1A_2$) ground state (Gritsan and Platz, 2006). This arylnitrene undergoes rapid intramolecular rearrangement to give benzazirine or ketenimine intermediates (Platz, 1995). When powerful nucleophiles are present, the ketenimine species reacts to form more polar azepine adducts. In the absence of nucleophiles, hydrolysis reactions can form the 3*H*-azepin-2-ol or the 1,3-dihydro-2*H*-azepin-2-one tautomers (Bou-Hamdan et al., 2011). Photo-irradiated samples of compound **1** showed that at least six new

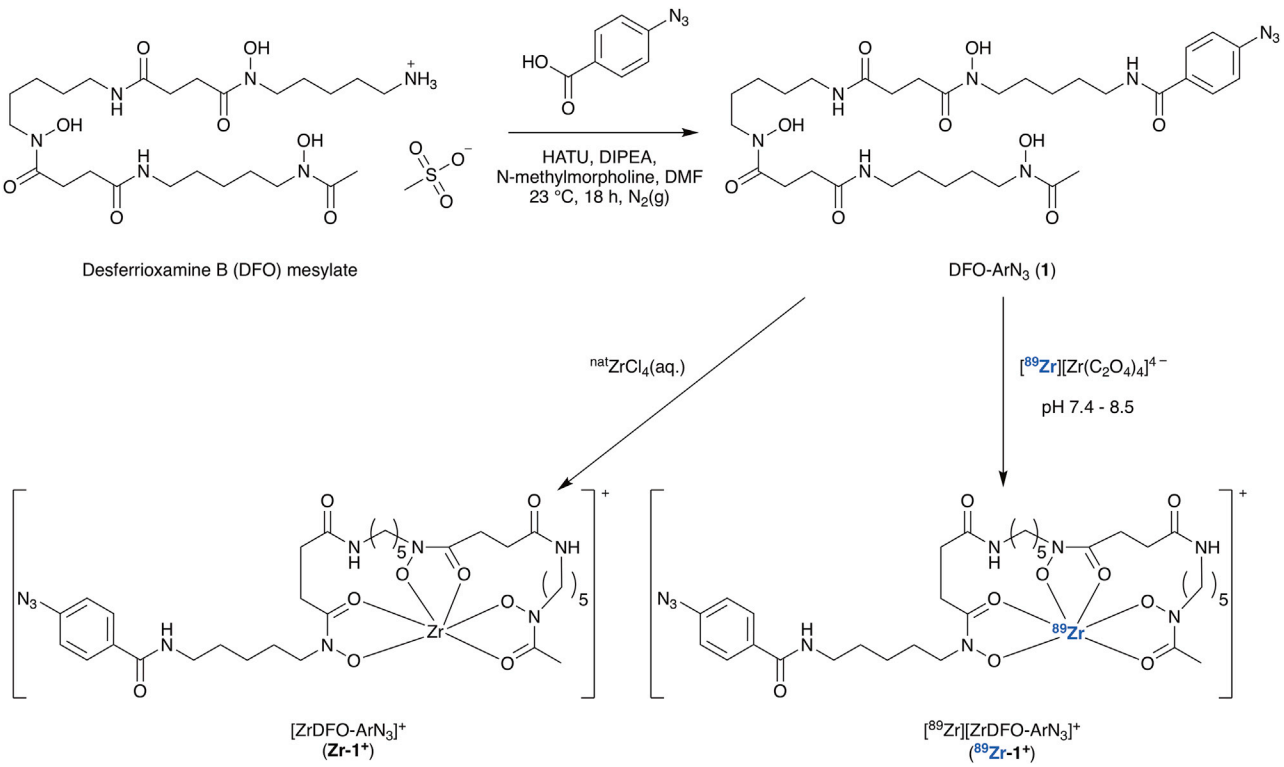

Scheme 2. Chemical Synthesis of DFO-ArN$_3$ (1) and Complexation of Zr^{4+} Ions to Give the Non-radioactive (Zr-1$^+$) and Radiolabeled ^{89}Zr-1$^+$) Coordination Complexes

species formed (Figure 2A). This observation is consistent with the mechanism of activation. The DFO ligand contains several nucleophilic groups (hydroxamates) that can induce intramolecular reactions with the ketenimine intermediate forming various cycles.

By integrating the peak in the UHPLC associated with compound **1**, it was possible to measure the photochemical degradation kinetics (Figure 2B). At room temperature, and using the LED (365 nm) at different intensities (25%, 50%, and 100%), the photochemical degradation of compound **1** fitted a first-order kinetic scheme (non-linear regression coefficient, R^2 >0.999 at each light intensity). Changes in the observed rate constant, k_{obs}/min^{-1}, were found to be linearly dependent on the light intensity (Figure 2C). These data are consistent with the anticipated photochemical response of molecules containing ArN$_3$ groups (Gritsan and Platz, 2006; Gritsan and Pritchina, 1992; Klán and Wirz, 2009).

Quantum Yield of Photochemical Activation

How efficient is photochemical activation of the ArN$_3$ in compound **1**? This question can be answered by determining the photochemical quantum yield (Φ), which is defined as the ratio of the number of reactions (n_r) to the number of photons absorbed (n_{abs}, Equation 1) (Klán and Wirz, 2009)

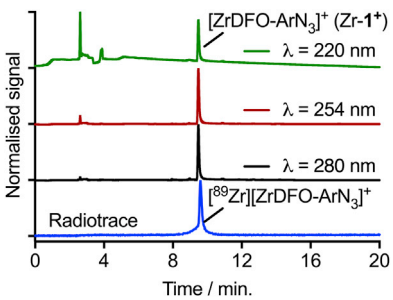

Figure 1. Radioactive UHPLC Characterization Data

UHPLC chromatograms showing quantitative radiolabeling to give [^{89}Zr][ZrDFO-ArN$_3$]$^+$ (^{89}Zr-**1**$^+$, blue trace, RCP >99%, RCC >99%) and electronic absorption chromatograms measured at 220 nm (green), 254 nm (red), and 280 nm (black) showing co-elution with an authenticated sample of non-radioactive Zr-**1**$^+$.

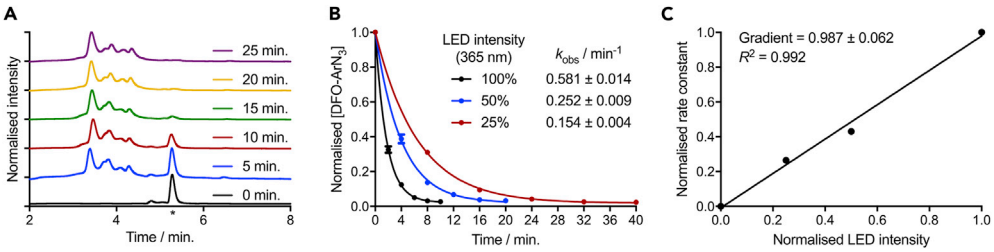

Figure 2. Kinetic Data on the Photochemically Induced Degradation of Compound 1 during Irradiation with UV Light (365 nm)

(A) Normalized UHPLC chromatograms recorded between 0 and 25 min (50% LED power). * Indicates starting material (compound **1**).

(B) Kinetic plot showing the change in concentration of compound **1** versus irradiation time (min.) using different LED intensities. Note, data are fitted with a first-order decay (R^2 >0.999 for each dataset), and the observed first-order rate constants, k_{obs}/min^{-1}, are shown in the inset. Error bars correspond to one standard deviation.

(C) Plot of the normalized observed rate constant versus the normalized LED intensity confirming that photodegradation is first order (gradient ~1.0) with respect to light intensity.

$$\Phi = \frac{n_r}{n_{abs}} \qquad \text{(Equation 1)}$$

An expression for the number of reactions at time t is given by the change in concentration (c) of the starting material multiplied by the volume (V, Equation 2).

$$n_r(t) = (c_0 - c(t)) \cdot V \qquad \text{(Equation 2)}$$

The molar photon flux $q^0_{m,\gamma}$ is defined as the number of photons in moles (i.e., in units of Einstein) incident on a sample per unit time and can be expressed as the light power ($P^0_{m,\gamma}$) divided by the product of Avogadro's constant (N_A) and the energy of each photon ($h\nu$) as given by Equation 3.

$$q^0_{m,\gamma} = \frac{P^0_{m,\gamma}}{N_A \cdot h\nu} \qquad \text{(Equation 3)}$$

The fraction of photons absorbed can be expressed as 1 minus the transmittance (T), which can be substituted for the measured absorbance using the Beer-Lambert law (Equation 4).

$$T(t) = 10^{-A(t)}, \quad \text{where} \quad A(t) = \varepsilon_\lambda\, c(t)\, d \qquad \text{(Equation 4)}$$

The differential photon absorption ($dn_\gamma(t)$) at a given time and wavelength (λ) can be calculated by Equation 5.

$$dn_{abs}(t) = q^0_{m,\lambda}\left[1 - 10^{-A(t)}\right]dt \qquad \text{(Equation 5)}$$

Finally, it follows that the quantum yield is given by Equation 6.

$$\Phi = \frac{(c_0 - c(t)) \cdot V}{\int_0^t q^0_{m,\lambda}\left[1 - 10^{-A(t)}\right]dt} \qquad \text{(Equation 6)}$$

Using experimental values from the kinetics of photochemical degradation of compound **1**, a photochemical quantum yield of 4.35% ± 0.43% was calculated. This means that around one in every ~23 photons that is absorbed (at ~365 nm) leads to photochemical activation via loss of N_2 as opposed to relaxation through other radiative or non-radiative (chemical quenching) pathways. These data indicated that photochemical activation of compound **1**, and other molecules functionalized with the ArN_3 group, is a highly efficient process.

Density Functional Theory Calculations

Next, to understand the thermochemical stability and photochemical reactivity of compound **1** in more detail, density functional theory (DFT) calculations were performed. The acyclic nature of compound **1** means that the compound has a large degree of conformational freedom. Therefore, to simplify calculation of the reaction coordinate and the electronic excitation profile, the non-substituted arylazide (benzylazide) was used as a model compound. All calculations used the uB3LYP/6-311++G(d,p) level of theory and included a polarizable continuum model (PCM, water). The calculated reaction coordinate is shown in

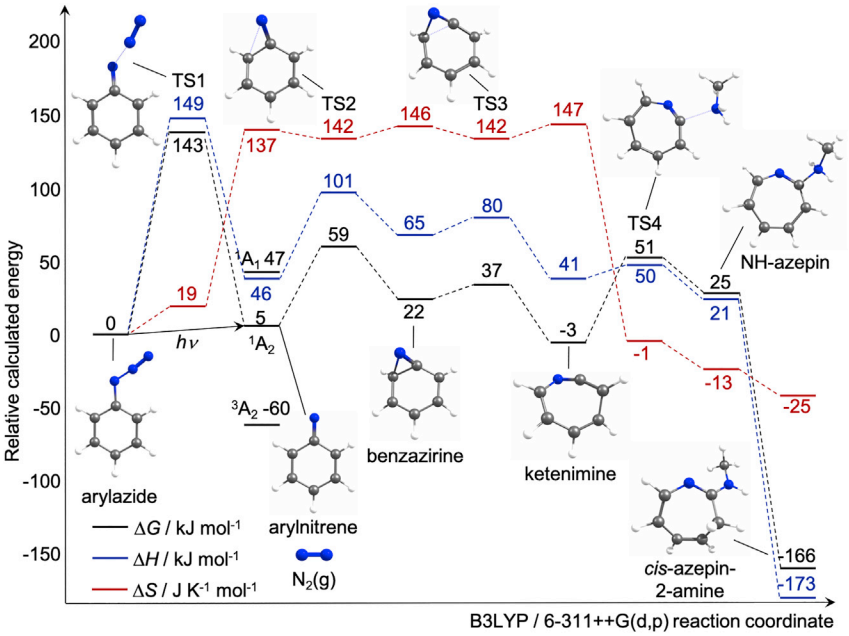

Figure 3. DFT-Calculated (uB3LYP/6-311++G(d,p)/PCM) Reaction Coordinate

The relative calculated differences in free energy (ΔG/kJ mol^{-1}), enthalpy (ΔH/kJ mol^{-1}), and entropy (ΔS/J K^{-1} mol^{-1}, at 298.15 K) of the various intermediates and transition states that connect arylazide (PhN_3) with the *N*-methyl-*cis*-azepin-2-amine product are shown. Photochemically induced reactivity of arylazides proceeds via the ground-state open-shell singlet nitrene ($^1A_2$ state) corresponding to the $(p_x)^1(p_y)^1$ electronic configuration where the *py* orbital on the N atom lies in the plane of the C_6H_5 ring. Note, owing to spin contamination, the energy of the $^1A_2$ state was estimated using the sum method by Ziegler et al. (Ziegler and Rank, 1977).

Figure 3. Relative changes in the reaction free energy, ΔG; enthalpy, ΔH; and entropy ΔS of each species, including all transition states between the arylazide starting material and the most stable geometric isomer formed (*cis*-*N*-methyl-3*H*-azepin-2-amine) after addition of methylamine to the ketenimine intermediate, are shown. In addition, relative energies of the possible electronic states of the arylnitrene were calculated.

The first feature to note is that formation of transition state 1 (TS1), which corresponds to loss of N_2 from arylazide, has a calculated free energy barrier of 143 kJ mol^{-1} in solution phase. This high barrier accounts for the thermal stability of the ArN_3 group and contributes to the prolonged shelf-life of chelates (like compound **1**) that are derivatized with ArN_3. Irradiation with UV light can circumvent this thermodynamic barrier (see the time-dependent DFT [TD-DFT)] section below) and leads to the formation of arylnitrene in the lowest energy open-shell singlet state ($^1A_2$). The $^1A_2$ ground state has a formal electronic configuration of $(p_x)^1(p_y)^1$ where the two unpaired electrons are primarily located in the *p*-orbitals of the nitrogen atom with some delocalization to the aromatic ring. Formation of the more stable triplet state ($^3A_2$) is spin forbidden, and the two closed-shell singlet states (both $^1A_1$ with either $(p_x)^2$ or $(p_y)^2$ electronic configurations centered on the N atom) are calculated to be higher in energy, with a low probability of populating these states at ambient temperature. The TS2 corresponding to the intramolecular rearrangement of arylnitrene has a calculated barrier of only $\Delta\Delta G_{TS2}$ = 54 kJ mol^{-1}, which includes destabilization from the loss of aromaticity. After ring insertion occurs, the benzazirine species (ΔG = 22 kJ mol^{-1}) isomerizes to give the more stable ketenimine intermediate (ΔG = −3 kJ mol^{-1}) via a relatively low-energy TS3 (ΔG = 37 kJ mol^{-1}). Nucleophilic attack by methylamine (CH_3NH_2) at the 2-position of the ketenimine intermediate proceeds via TS4 (ΔG = 51 kJ mol^{-1}) and initially produces the NH-azepin adduct. This NH-azepin then isomerizes to yield the *cis*-azepin-2-amine product. Formation of the azepin-2-amine from benzylazide and methylamine is calculated to be thermodynamically spontaneous with an overall reaction free energy of ΔG = −166 kJ mol^{-1}. As expected, the main driving force for the initial photoactivation is entropic (N_2(g) release, ΔS = +137 J^{-1} K^{-1} mol^{-1}). However, nucleophilic addition to the ketenimine, and similarly, conjugation of a photoactive chelate to a biologically active molecule, is driven primarily by changes in enthalpy (ΔH = −173 kJ mol^{-1}).

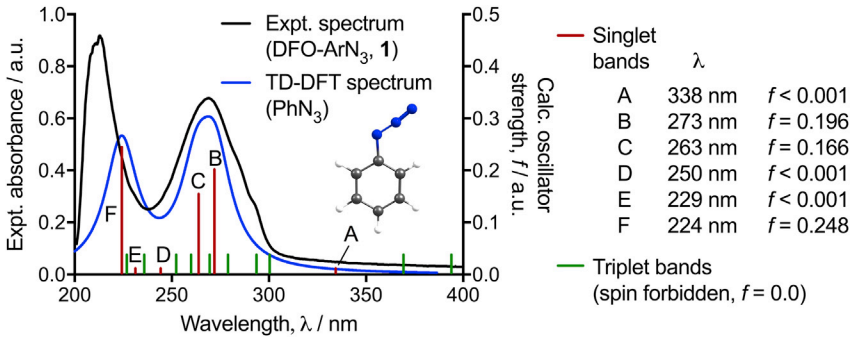

Figure 4. Experimental Electronic Absorption Spectroscopy and Time-Dependent DFT

Overlay of the experimentally measured electronic absorption spectrum of compound **1** and the TD-DFT (uB3LYP/6-311++G(d,p)/PCM)-calculated spectrum of the model compound arylazide (PhN_3). Note that the calculated spectrum was produced by using Lorentzian broadening, 20-nm full-width at half maximum. Calculated energies and oscillator strengths (*f*/a.u.) of the bands corresponding to transitions to the first six excited singlet states with non-zero expectation values are shown by vertical red lines (band details inset). For reference, band energies to the excited triplet states are shown by vertical green lines. The simulated spectrum and all calculated energies are *x*-shifted by +12 nm for clarity. Molecular orbital contributions involved in the excitation to the main singlet bands are presented in Table S1.

TD-DFT calculations were used to probe the electronic nature of the photoactivation of arylazide. An overlay of the experimentally measured electronic absorption spectrum of compound **1** (in MeOH) and the TD-DFT-calculated spectrum is presented in Figure 4 (see also Transparent Methods Figure S8 and Table S1). Perhaps surprisingly, compound **1**, and indeed arylazide compounds like 4-azidobenzoic acid show almost no absorbance at wavelengths above ~325 nm. Measurements of the molar absorption coefficients at 365 and 395 nm gave values of $16.9 \pm 1.9\ M^{-1}\ cm^{-1}$ and $5.2 \pm 1.3\ M^{-1}\ cm^{-1}$, respectively. Nevertheless, TD-DFT calculations of the 16 lowest energy excited states (including both singlets and triplets) of arylazide confirmed that excitation bands are present in the wavelength range used to promote the photochemistry. Electronic transitions to six major singlet excited states (assigned as bands A to F) contribute to the measured absorption profile of compound **1** in the region 200–600 nm. Note that at shorter wavelengths, the fit between the calculated and the experimental spectrum is less accurate because of the use of the model arylazide and the continuum solvation model, which do not account for the full electronic complexity or solvation dynamics of compound **1**. However, experimental features associated with absorption at wavelengths >250 nm are well reproduced.

TD-DFT calculations allow deconvolution of the change in the electronic density associated with the formation of a particular excited state in terms of electronic mixing between the ground-state molecular orbitals (MOs) (Figure 5, and Transparent Methods Table S1). MO analysis from TD-DFT calculations performed on benzylazide found that absorption band A (corresponding to excitation to the lowest energy excited singlet state) involves 96.4% mixing of the electron density from the highest occupied MO to the lowest unoccupied molecular orbital (LUMO). Inspection of the MO isosurfaces showed that this transition involves primarily transfer of electron density from a populated $\pi\pi^*$ orbital of the benzyl ring to the unoccupied, in-plane antibonding $p\pi^*$ orbital centered on the azide group. Populating this excited state weakens the azide bond and stimulates N_2 dissociation. Interestingly, our experimental observations indicate that any wavelength that populates the first excited singlet state can induce arylazide activation. However, test experiments using a shorter-wavelength LED (~275 nm), which populates the second or third excited singlet states (bands B and C, respectively), found negligible photochemical activation of the ArN_3 group (data not shown). This observation is consistent with the TD-DFT calculations, which indicate that bands B and C involve electronic transitions to higher-energy virtual orbitals (LUMO+1 and above). Kasha's rule suggests that relaxation of second and third excited singlet states of ArN_3 should populate the LUMO, but inspection of the MOs shows that this process is symmetry forbidden (Figure 5).

Two-Step Photochemical Conjugation and ^{89}Zr-Radiolabeling of Trastuzumab

Before investigating a simultaneous one-pot photoradiochemical process, experiments were performed using the traditional two-step approach. This route involved the photochemical conjugation between compound **1** and trastuzumab, followed by ^{89}Zr-radiolabeling (Scheme 3, bottom pathway). The photochemical

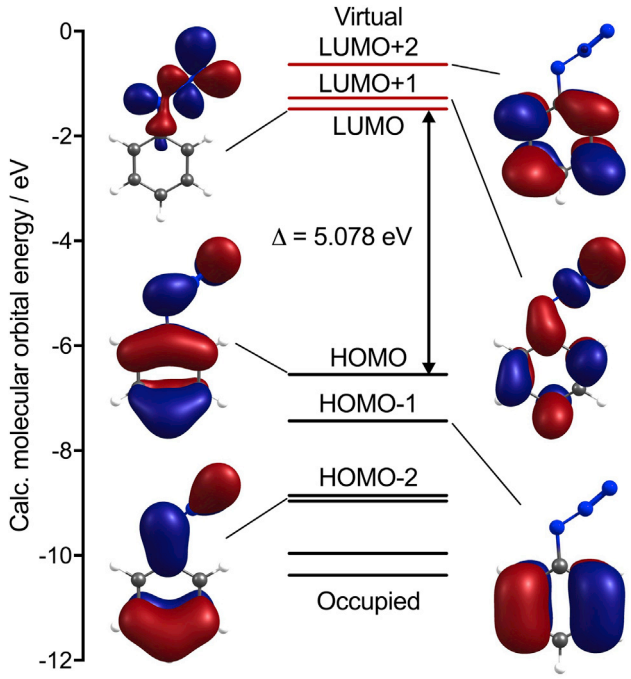

Figure 5. Molecular Orbital Diagram of ArN_3

DFT-calculated (B3LYP/6-311++G(d,p)/PCM) molecular orbital diagram. Electron density isosurfaces of the three highest occupied molecular orbitals (HOMOs) and three lowest unoccupied molecular orbitals (LUMOs) for the model compound arylazide (PhN_3) are shown. Note that the isosurfaces were generated by using a contour value of 0.035 and correspond to 96.5% of the total electron density.

conjugation was performed at room temperature for 25 min using a Rayonet reactor. The DFO-azepin-trastuzumab conjugate was purified by using a combination of size exclusion chromatography (SEC) methods including spin column centrifugation and preparative PD-10 gel filtration. DFO-azepin-trastuzumab was then radiolabeled with ^{89}Zr using standard conditions (Holland et al., 2010b, 2010a; 2012; Rylova et al., 2016; Verel et al., 2003a, 2003b; Vosjan et al., 2010). Aliquots of the crude radiolabeling mixture were retained, and then the product was purified and formulated in sterile PBS by using standard SEC methods. Analytical measurements on the crude and purified samples of [^{89}Zr]ZrDFO-azepin-trastuzumab were performed using radioactive instant thin-layer chromatography (radio-iTLC), analytical PD-10-SEC, and radioactive SEC-UHPLC (Figure 6).

Experiments confirmed that the DFO-azepin-trastuzumab was radiolabeled efficiently with ^{89}Zr giving a crude radiochemical conversion (RCC) of >98% after incubating the mixture at room temperature for 15 min. On scaling up the radiolabeling reaction for use in cellular and animal experiments, the final radiochemical yield (RCY) of the purified sample was >99%, and the radiochemical purity (RCP) was measured at >99.5% by analytical PD-10-SEC and >98% by SEC-UHPLC. For the preparations used in the animal studies, the final activity concentration was 29.7 MBq mL^{-1}, with a decay-corrected molar activity (A_m) of 13.7 MBq nmol^{-1} of protein for the stock sample used in the normal doses (*vide infra*).

Further ^{89}Zr-radiolabeling experiments were performed to measure the radiolabeling kinetics and overall RCC yields of DFO-azepin-trastuzumab samples that were prepared using different initial chelate-to-mAb ratios in the photochemical conjugation step (Figure 7 and Transparent Methods Figure S11). For each sample, the radiolabeling kinetics was monitored by radio-iTLC (Figure 7A) and the RCC (%) versus time was plotted (Figure 7B). These experiments showed a linear relation between the initial chelate-to-mAb ratio and the overall RCC at equilibrium (time points >60 min, Figure S11). Using these data, combined with the experimentally determined molar activity of the stock solution of [^{89}Zr][Zr(C_2O_4)$_4$]$^{4-}$ (measured by titration with DFO) (Rylova et al., 2016) the photochemical conjugation efficiency between DFO-ArN_3 (**1**) and trastuzumab was estimated to be 3.5% ± 0.4% (n = 3). Hence, for the samples used in the biological

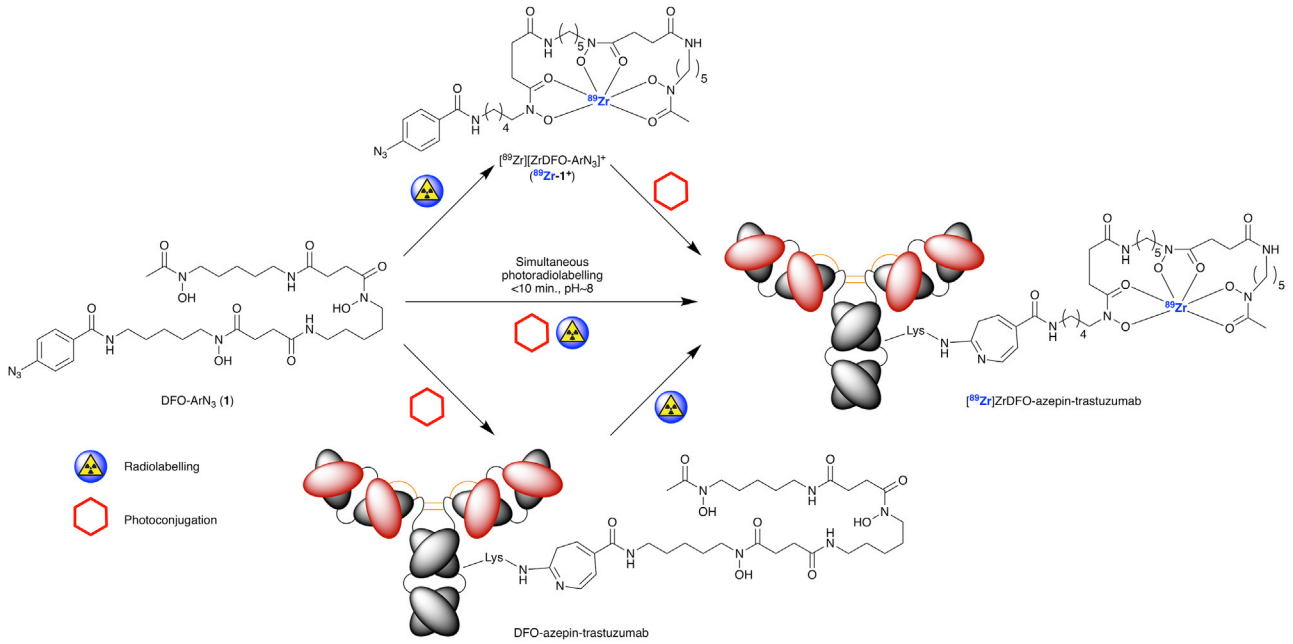

Scheme 3. Photoradiochemical Synthesis of [^{89}Zr]ZrDFO-Azepin-Trastuzumab via Three Separate Routes

(Top) Pre-radiolabelling and subsequent photochemical conjugation of [^{89}Zr]ZrDFO-ArN$_3$ (^{89}Zr-**1**$^+$) with the antibody. (Middle) Simultaneous one-step photoradiochemical labeling. (Bottom) Two-step photochemical conjugation of the antibody and subsequent ^{89}Zr radiolabeling of the isolated DFO-azepin-trastuzumab intermediate.

studies, an initial chelate-to-mAb ratio of 26.4:1 yielded ~0.85 accessible chelates per mAb in the final product.

The radiochemical stability of [^{89}Zr]ZrDFO-azepin-trastuzumab with respect to change in the RCP during incubation in human serum at 37 °C for up to 92 h was determined by SEC-UHPLC (Figure 7C). Experiments confirmed that the ^{89}Zr activity remained bound to the mAb (<2% decrease in RCP after 92 h) with essentially no transchelation serum proteins (transferrin, albumin, etc.).

Cellular Saturation Binding Assays (Immunoreactivity)

The biochemical viability of [^{89}Zr]ZrDFO-azepin-trastuzumab was measured by using standard cellular saturation binding assays in accordance with the methods introduced by Lindmo et al.(Junghans, 1999; Konishi

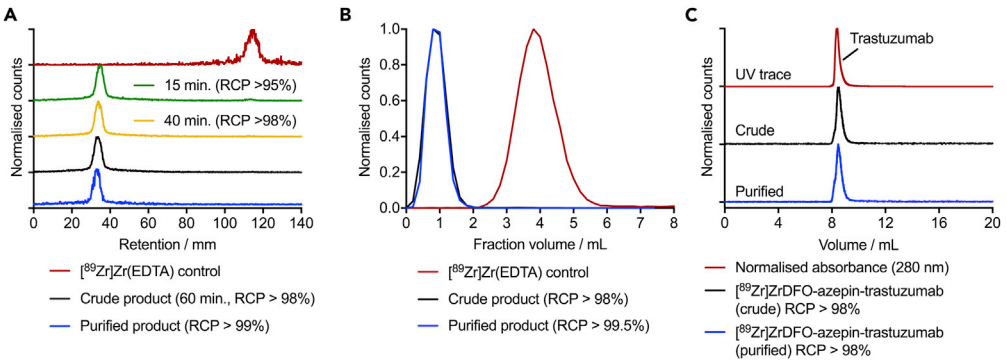

Figure 6. Characterization Data for the Radiochemical Synthesis of [^{89}Zr]ZrDFO-Azepin-Trastuzumab

(A) Radio-iTLC chromatograms showing [^{89}Zr]ZrEDTA control; the crude reaction mixture at 15, 40, and 60 min; and the purified product.

(B and C) (B) Analytical PD-10-SEC elution profiles, and (C) SEC-UHPLC chromatograms of the crude and purified product.

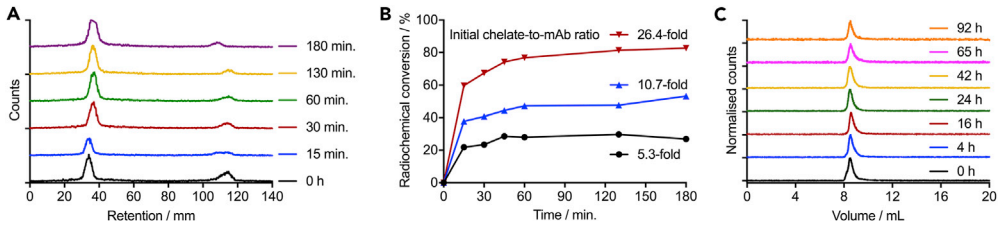

Figure 7. [^{89}Zr]ZrDFO-azepin-trastuzumab Radiolabeling Kinetics and Stability Data

(A) Radio-iTLC chromatograms showing the kinetics of formation of [^{89}Zr]ZrDFO-azepin-trastuzumab versus time using a pre-functionalized DFO-azepin-trastuzumab sample prepared with an initial chelate-to-mAb ratio of 26.4:1. Data for reactions starting with different initial chelate-to-mAb ratios are presented in Figure S11.

(B) Plot of the percentage radiochemical conversion (RCC) versus time using samples of DFO-azepin-trastuzumab pre-conjugated at different initial chelate-to-mAb ratios.

(C) Radioactive SEC-UHPLC confirming that [^{89}Zr]ZrDFO-azepin-trastuzumab remains stable with respect to change in radiochemical purity during incubation in human serum at 37 °C for 92 h.

et al., 2004; Lindmo et al., 1984). The human ovarian cancer cell line SK-OV-3 shows high expression of the human epidermal growth factor receptor 2 (HER2/*neu*), which is the target protein of trastuzumab. Saturation binding experiments confirmed that the protein remained biochemically active with an estimated immunoreactivity fraction between 63% and 74% (n = 2, Figure 8). Note that these cellular assays were incubated for only 1 h and the slightly low value of the immunoreactivity is primarily associated with slow binding kinetics. Nevertheless, the immunoreactive fraction is comparable to the reported value of 87% ± 7% obtained with [^{89}Zr]ZrDFO-Nsucc-trastuzumab that was conjugated using one of the standard thermochemical routes (*N*-succinyl activated ester) (Holland et al., 2010a).

Small-Animal PET Imaging and Biodistribution Studies

After confirming that [^{89}Zr]ZrDFO-azepin-trastuzumab was chemically stable and biochemically active *in vitro*, the pharmacokinetics and target specificity were evaluated in athymic nude mice bearing subcutaneous SK-OV-3 tumors. PET images were recorded at multiple time points between 2 and 94 h post-administration. Two groups of mice were used. The normal group (n = 5) received a high molar activity formulation (13.7 MBq nmol^{-1}), and the blocking group received the same amount of radioactivity but a reduced molar activity of 0.14 MBq nmol^{-1}. Representative PET images showing coronal and axial planes taken through the center of the tumors are presented in Figure 9 (see also Transparent Methods Figures S12 and S13). PET imaging data were also quantified by drawing volumes-of-interest over various tissues and plotting the data as time-activity bar charts (Figure 10, based on quantification of the images in units of percentage injected dose per gram (%ID g^{-1}), and Figure S14 for equivalent data using image quantification in units of the mean standardized uptake value). The pharmacokinetic profile and tumor uptake of [^{89}Zr]ZrDFO-azepin-trastuzumab was consistent with previously reported experiments using ^{89}Zr-DFO-radiolabeled trastuzumab produced via traditional coupling chemistries (Holland et al., 2010a).

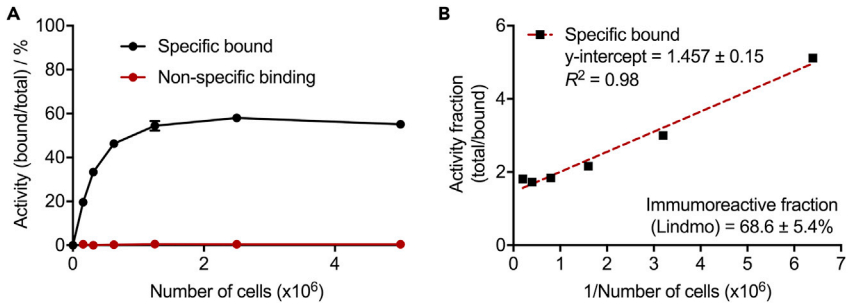

Figure 8. Measurement of the Immunoreactive Fraction of [^{89}Zr]ZrDFO-Azepin-Trastuzumab as Determined by Cellular Binding to SK-OV-3 (HER2/*neu* positive) Cells

(A) Saturation binding plot. Error bars correspond to one standard deviation.

(B) Lindmo plot.

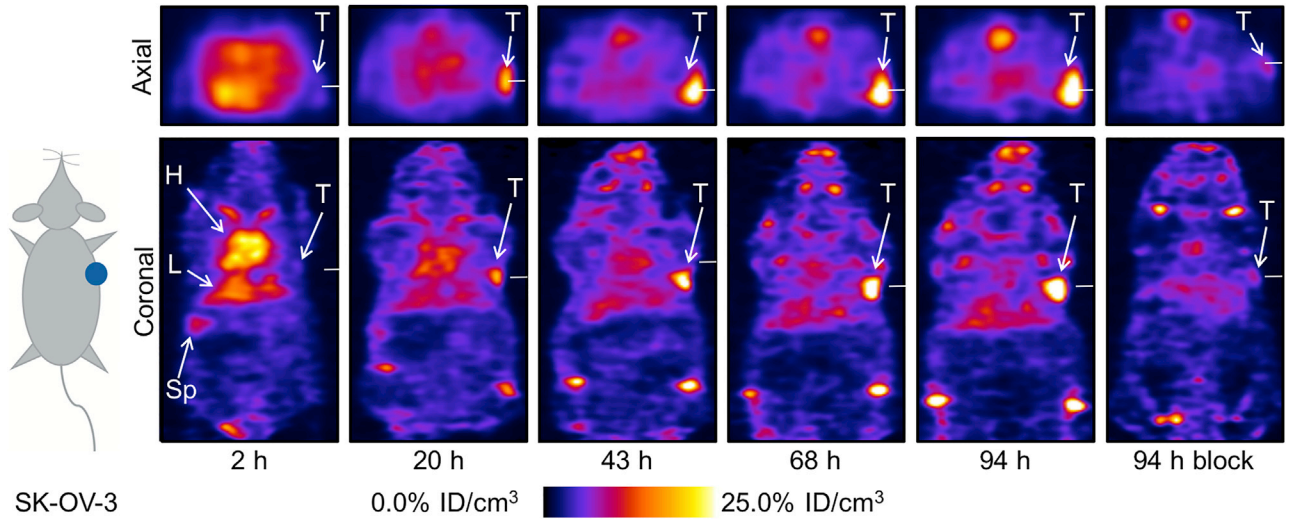

Figure 9. Temporal [^{89}Zr]ZrDFO-Azepin-Trastuzumab PET Images Recorded in Mice Bearing SK-OV-3 Tumors on the Right Flank
T, tumor; H, heart; L, liver; Sp, spleen

The effective half-life ($t_{1/2}$(eff)/h) of [^{89}Zr]ZrDFO-azepin-trastuzumab was measured in mice by using a calibrated dosimeter (Transparent Methods Figure S15). A value of $t_{1/2}$(eff) = 45.7 ± 7.7 h was measured (n = 11; R^2 ~ 0.99) with an estimated biological half-life, $t_{1/2}$(biol.) = 109.5 ± 18.4 h. No difference was observed between the normal and blocking groups. These data are consistent with previous reports on ^{89}Zr-radiolabeled trastuzumab (Dijkers et al., 2009; Holland et al., 2010a).

After the final imaging time point, animals were euthanized and a biodistribution analysis was performed to obtain accurate quantification of the accumulation of ^{89}Zr in different tissues (Figure 11, Table 1 and Transparent Methods Figures S16–S19). Comparison of the biodistribution data between the normal and blocking groups showed a specific accumulation of radioactivity in the tumor (65.8% ± 14.2 %ID g^{-1} in the normal group versus 12.1% ± 4.1%ID g^{-1} in the blocking group, p value = 0.0006). With the exception of the activity retained in the blood pool (7.4% ± 1.0 %ID g^{-1} for the normal versus 4.8% ± 1.2 %ID g^{-1} for the blocking group [p value = 0.003]), no statistically significant differences were observed between radioactivity accumulation in the background tissues of the two groups of mice. Furthermore, a comparison of the tumor-to-tissue contrast ratios recorded from the biodistribution studies performed on the photoradiochemical product [^{89}Zr]ZrDFO-azepin-trastuzumab and on [^{89}Zr]ZrDFO-Nsucc-trastuzumab produced by a conventional conjugation route showed no statistically significant differences between the two radiotracers (Transparent Methods Figure S20).(Holland et al., 2010a) Collectively, the data from experiments performed *in vitro*, *in vivo*, and *ex vivo* indicate that the photoradiochemical route to ^{89}Zr-radiolabeled trastuzumab yields a radiolabeled compound that is of equivalent quality to other ^{89}Zr-mAbs produced via established methods.

Simultaneous Photoradiolabeling of Trastuzumab

Previously, we demonstrated that the photoradiochemical approach was successful when radiolabeling either pre-purified mAbs or fully formulated samples (Herceptin) (Patra et al., 2019). In addition to fast reaction and processing times, a one-pot procedure has the unique advantage of avoiding the need to isolate and characterize the conjugated intermediate antibodies. To illustrate the feasibility of the simultaneous photoradiochemical process, experiments were performed to produce [^{89}Zr]ZrDFO-azepin-trastuzumab in a single step.

Reactions were established in which [^{89}Zr][Zr(C_2O_4)$_4$]$^{4-}$, compound **1**, and trastuzumab (at an initial chelate-to-mAb ratio of ~29:1) were mixed in water and the pH adjusted to ~8–9. Control reactions were performed in the absence of either the chelate (**1**) or the mAb. Mixtures were stirred gently at room temperature and irradiated using the LED source (365 or 395 nm) for 10 min. Note that in this case stirring appeared to be more important than in our previous experiments with ^{68}Ga (Patra et al., 2019). After irradiation, the reactions were quenched by

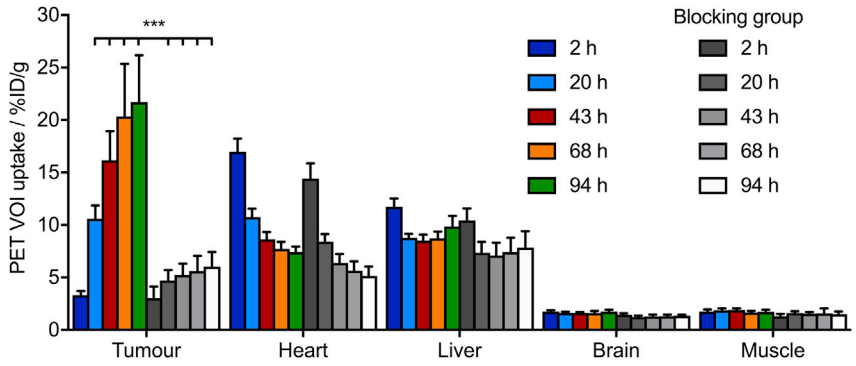

Figure 10. Time-Activity Bar Chart Showing the Activity Associated with Different Tissues (volumes of Interest, VOI) versus Time

Data presented are based on quantification of the PET images in units of %ID cm^{-3}. Equivalent data using quantification of the PET images in terms of the mean standardized uptake value are shown in Figure S14. Error bars correspond to one standard deviation.

the addition of diethylenetriamine pentaacetic acid (DTPA). Aliquots of the crude samples were retained, and a fraction was purified by SEC methods. Crude and purified samples were then analyzed by using radio-iTLC, analytical PD-10-SEC, and SEC-UHPLC methods (Figure 12 and Transparent Methods Table S3).

Analysis of the crude reaction mixtures also indicated that ~72%–73% (n = 2, by analytical PD-10-SEC) and ~67%–88% (n = 2, by SEC-UHPLC) of the ^{89}Zr-radioactivity was associated with trastuzumab. Control reactions confirmed that the ^{89}Zr radioactivity bound to trastuzumab specifically (Figures 12A and 12B, green and yellow traces). After purification, simultaneous photoradiolabeling gave [^{89}Zr]ZrDFO-azepin-trastuzumab with a decay-corrected RCY of ~76%, a RCP ~97% (measured by SEC-UHPLC), and a molar activity of 0.41 MBq $nmol^{-1}$ of protein (n = 2). Interestingly, both the 365- and 395-nm LED sources gave equivalent radiochemical conversions. Reactions were complete in <10 min, and the entire process, from non-labeled trastuzumab to formulated [^{89}Zr]ZrDFO-azepin-trastuzumab, was accomplished in <15 min. With a higher intensity light source, it is conceivable that the photoradiochemical synthesis could be accomplished in a few seconds, which would mean that radiotracer production times are limited only by the time required for purification and quality control.

Comparison of the final RCYs measured between the two-step process and the simultaneous (one-step) process indicate that the photochemical conjugation efficiency increased from 3.5% to ~76%. This result

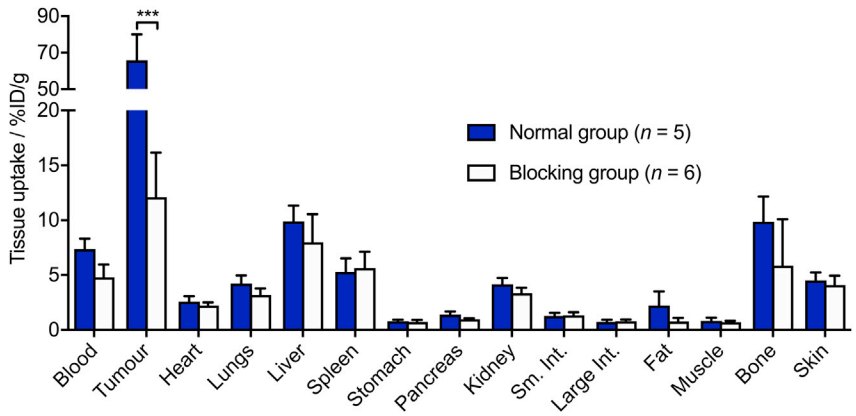

Figure 11. Bar Chart Showing *Ex Vivo* Biodistribution Data (%ID/g) for the Uptake of [^{89}Zr]ZrDFO-Azepin-Trastuzumab in Mice Bearing Subcutaneous SK-OV-3 Tumors

Data were recorded after the final imaging time point at 94 h post-injection. ***Student's t test p value < 0.001. An equivalent plot using units of standardized uptake value is presented in Figure S17. Data showing tumor-to-tissue contrast ratios are presented in Figure S18. Error bars correspond to one standard deviation.

Tissue	Normal Group (n = 5)		Blocking Group (n = 6)	
	[^{89}Zr]ZrDFO-Azepin-Trastuzumab (94 h)/%ID g^{-1} ± SD[a]	Tumor-to-Tissue Contrast Ratio ± SD[b]	[^{89}Zr]ZrDFO-Azepin-Trastuzumab (94 h)/%ID g^{-1} ± SD[a]	Tumour-to-Tissue Contrast Ratio ± SD[b]
Blood	7.36 ± 0.96	8.94 ± 2.25	4.79 ± 1.18	2.53 ± 1.05
Tumor	65.79 ± 14.19	1.00	12.10 ± 4.06	1.00
Heart	2.58 ± 0.49	25.51 ± 7.32	2.22 ± 0.28	5.45 ± 1.95
Lungs	4.22 ± 0.75	15.57 ± 4.35	3.17 ± 0.60	3.82 ± 1.47
Liver	9.90 ± 1.44	6.64 ± 1.73	7.99 ± 2.56	1.51 ± 0.70
Spleen	5.28 ± 1.24	12.45 ± 3.97	5.64 ± 1.48	2.14 ± 0.91
Stomach	0.79 ± 0.15	83.03 ± 23.85	0.74 ± 0.19	16.36 ± 6.95
Pancreas	1.39 ± 0.28	47.27 ± 13.91	0.98 ± 0.10	12.39 ± 4.37
Kidney	4.16 ± 0.57	15.82 ± 4.03	3.35 ± 0.50	3.61 ± 1.33
Small intestine	1.28 ± 0.28	51.30 ± 15.70	1.33 ± 0.28	9.13 ± 3.62
Large intestine	0.74 ± 0.20	88.79 ± 30.95	0.79 ± 0.17	15.29 ± 6.10
Fat	2.22 ± 1.29	29.61 ± 18.31	0.78 ± 0.32	15.49 ± 8.24
Muscle	0.82 ± 0.30	79.84 ± 33.39	0.71 ± 0.12	17.05 ± 6.39
Bone	9.86 ± 2.29	6.67 ± 2.12	5.85 ± 4.24	2.07 ± 1.65
Skin	4.51 ± 0.73	14.58 ± 3.94	4.09 ± 0.86	2.96 ± 1.17

Table 1. *Ex Vivo* Biodistribution Data for [^{89}Zr]ZrDFO-Azepin-Trastuzumab in Mice Bearing SK-OV-3 Tumors

[a]Uptake data are expressed as the mean %ID g^{-1} ± one standard deviation (SD).

[b]Errors for the tumor-to-tissue ratios are calculated as the geometric mean of the standard deviations.

shows that the chemical efficiency of simultaneous photoradiolabeling is comparable to many of the most efficient thermally mediated methods, which typically display ~60%–80% conjugation efficiency (Holland et al., 2010b, 2010a; 2012; Rylova et al., 2016; Verel et al., 2003a, 2003b; Vosjan et al., 2010). Under the conditions employed it is likely that the kinetics of metal ion complexation is equal to, or faster than, that of the photochemical conjugation step. Complexation of $^{89}Zr^{4+}$ ions by the DFO-ArN_3 chelate reduces the probability of intramolecular reactions between the nucleophilic hydroxamate groups and the photo-generated intermediates. Hence, pre-complexation increases the photochemical conjugation efficiency when compared with the free chelate (**1**). Notably, the photoradiochemical method is also suitable for use in fully automated radiochemical synthesis modules. Automated photoradiochemical synthesis has the potential to change the way in which radiolabeled mAbs, immunoglobulin fragments, and other proteins are produced in the clinic.

Conclusions

Experiments demonstrated that the photoradiolabeling methods are viable for the synthesis of radiolabeled antibodies for immuno-PET. In contrast to existing (thermochemical) technologies, photoradiochemistry allows for the rapid synthesis of [^{89}Zr]ZrDFO-azepin-trastuzumab in high radiochemical yield and purity using a simultaneous, one-pot approach. Accessing radiolabeled proteins directly from the non-functionalized source eliminates the need to isolate and characterize a radiolabeling precursor (here DFO-azepin-trastuzumab). Our work illustrates the potential of applying photochemistry in radiopharmaceutical science. We continue to investigate the use of photoradiochemistry with different photoactivatable groups, chelates, and radionuclides for producing

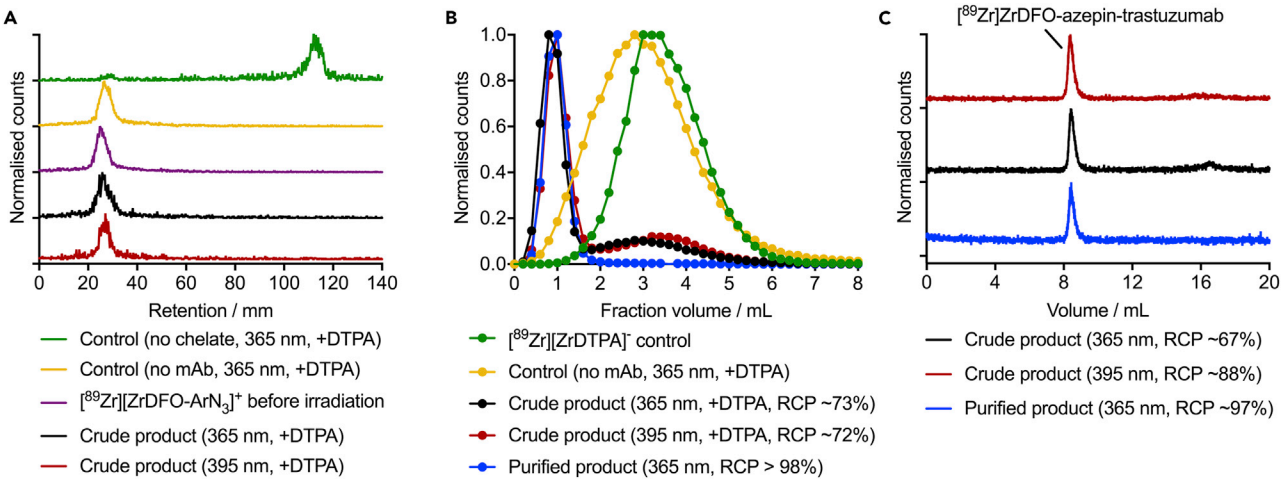

Figure 12. Characterization Data for the Simultaneous One-Pot Photoradiochemical Synthesis of [^{89}Zr]ZrDFO-Azepin-Trastuzumab

(A and B) (A) Radio-iTLC chromatograms showing control reactions in the absence of compound **1** (no chelate, green) or mAb (yellow), ^{89}Zr-**1**$^{+}$ before irradiation (purple), and the crude products after irradiation with 365 nm (black) and 395 nm (red). (B) Analytical PD-10-SEC elution profiles showing the [^{89}Zr][ZrDTPA]$^{-}$ control (green, equivalent to the no chelate control confirming no non-specific binding of $^{89}Zr^{4+}$ ions to the mAb), a control reaction without mAb (yellow), crude reaction mixtures after irradiation and DTPA quenching at 365 nm (black) and 395 nm (red), and the purified product (blue).
(C) SEC-UHPLC chromatograms of the crude and purified product.

diagnostic and therapeutic radiopharmaceuticals based on proteins, peptides, small molecules, and nanoparticles.

Limitations of the Study

Although photoradiochemistry offers an exciting alternative for the synthesis of radiolabeled proteins, and we have shown that photoradiochemistry can facilitate processes that are not achievable using standard thermochemical methods, some limitations exist. Namely, the success of the photoradiochemical reaction is dependent on the experimental geometry. The light-activation process was found to be highly efficient, but experimentally, the shape and focus point of the light beam, the photon flux, and the potential absorption or scattering from the reaction vessel or chemical components of the reaction mixture mean that care must be taken to achieve reproducible results. Similar to standard thermochemical methods, we have also discovered that the photochemical conjugation efficiency depends on the nature of the photoactive group, the chelate or complex, and also other factors including the protein, solvent composition, mixing efficiency, and concentration-dependent radiochemical kinetics (Holland, 2018). Much work is required before photoradiochemical methods can be standardized.

METHODS

All methods can be found in the accompanying Transparent Methods supplemental file.

SUPPLEMENTAL INFORMATION

Supplemental Information can be found online at https://doi.org/10.1016/j.isci.2019.03.004.

ACKNOWLEDGMENTS

J.P.H. thanks the Swiss National Science Foundation (SNSF Professorship PP00P2_163683), the Swiss Cancer League (Krebsliga Schweiz; KLS-4257-08-2017), and the University of Zurich (UZH) for financial support. This project has received funding from the European Union's Horizon 2020 research and innovation program and from the European Research Council under the Grant Agreement No 676904, ERC-StG-2015, NanoSCAN. We thank all members of the Radiochemistry and Imaging Science group at UZH for helpful discussions. We thank Dr. Benjamin Probst for spectroradiometric measurements. J.P.H. thanks Dr. Douglas J. Fox from Gaussian Inc. for helpful discussions regarding DFT calculations.

AUTHOR CONTRIBUTIONS

Conceptualization, J.P.H.; Methodology, J.P.H., M.P., S.K., and L.S.E.; Investigation, J.P.H., M.P., S.K., and L.S.E.; Formal Analysis, J.P.H., M.P., and S.K.; Resources, J.P.H.; Writing – Original Draft, J.P.H.; Writing – Review and Editing, J.P.H., M.P., and S.K.; Visualization, J.P.H.; Supervision, J.P.H.; Project Administration, J.P.H.; Funding Acquisition, J.P.H.

DECLARATION OF INTERESTS

J.P.H. and M.P. are listed as inventors on a patent application related to the materials and methods used in this work. Otherwise, the authors declare no competing interests.

Received: December 12, 2018
Revised: January 29, 2019
Accepted: March 2, 2019
Published: March 29, 2019

REFERENCES

Bayley, H., and Knowles, J.R. (1977). Photoaffinity labeling. Methods Enzymol. *46*, 69–114.

Borden, W.T., Gritsan, N.P., Hadad, C.M., Karney, W.L., Kemnitz, C.R., and Platz, M.S. (2000). The interplay of theory and experiment in the study of phenylnitrene. Acc. Chem. Res. *33*, 765–771.

Boros, E., and Holland, J.P. (2018). Chemical aspects of metal ion chelation in the synthesis and application antibody-based radiotracers. J. Label. Compd. Radiopharm. *61*, 652–671.

Bou-Hamdan, F.R., Lévesque, F., O'Brien, A.G., and Seeberger, P.H. (2011). Continuous flow photolysis of aryl azides: preparation of 3H-azepinones. Beilstein J. Org. Chem. *7*, 1124–1129.

Chowdhry, V., and Westheimer, F.H. (1979). Photoaffinity labeling of biological systems. Annu. Rev. Biochem. *48*, 293–325.

Dennler, P., Fischer, E., and Schibli, R. (2015). Antibody conjugates: from heterogeneous populations to defined reagents. Antibodies *4*, 197–224.

Dijkers, E.C.F., Kosterink, J.G.W., Rademaker, A.P., Perk, L.R., van Dongen, G.A.M.S., Bart, J., de Jong, J.R., de Vries, E.G.E., and Lub-de Hooge, M.N. (2009). Development and characterization of clinical-grade 89Zr-trastuzumab for HER2/neu immunopet imaging. J. Nucl. Med. *50*, 974–981.

Eichenberger, L.S., Patra, M., and Holland, J.P. (2019). Photoactive chelates for radiolabelling proteins. Chem. Commun. (Camb). *55*, 2257–2260.

Gritsan, N., and Platz, M. (2010). Photochemistry of Azides: the azide/nitrene interface. In Organic Azides: Syntheses and Applications, S. Bräse and K. Banert, eds. (John Wiley & Sons), pp. 311–372.

Gritsan, N.P., and Platz, M.S. (2006). Kinetics, spectroscopy, and computational chemistry of arylnitrenes. Chem. Rev. *106*, 3844–3867.

Gritsan, N.P., and Pritchina, E.A. (1992). Mechanism of the photolysis of aromatic azides. Russ. Chem. Rev. *61*, 500–516.

Hashizume, K., Hashimoto, N., and Miyake, Y. (1995). Synthesis of positron labeled photoactive compounds:18F labeled aryl azides for positron labeling of biochemical molecules. J. Org. Chem. *60*, 6680–6681.

Holland, J.P. (2018). Chemical kinetics of radiolabelling reactions. Chem. Eur. J. *24*, 16472–16483.

Holland, J.P., and Vasdev, N. (2014). Charting the mechanism and reactivity of zirconium oxalate with hydroxamate ligands using density functional theory: implications in new chelate design. Dalton Trans. *43*, 9872–9884.

Holland, J.P., Divilov, V., Bander, N.H., Smith-Jones, P.M., Larson, S.M., and Lewis, J.S. (2010b). 89Zr-DFO-J591 for immunoPET imaging of prostate-specific membrane antigen (PSMA) expression in vivo. J. Nucl. Med. *51*, 1293–1300.

Holland, J.P., Caldas-Lopes, E., Divilov, V., Longo, V.A., Taldone, T., Zatorska, D., Chiosis, G., and Lewis, J.S. (2010a). Measuring the pharmacodynamic effects of a novel Hsp90 inhibitor on HER2/neu expression in mice using 89Zr-DFO-trastuzumab. PLoS One *5*, e8859.

Holland, J.P., Evans, M.J., Rice, S.L., Wongvipat, J., Sawyers, C.L., and Lewis, J.S. (2012). Annotating MYC status with 89Zr-transferrin imaging. Nat. Med. *18*, 1586–1591.

Junghans, R.P. (1999). Cruel antibody fictions! Cellular antigen enumeration by "saturation" binding. Immunol. Today *20*, 401–406.

Klán, P., and Wirz, J. (2009). Photochemistry of Organic compounds: from concepts to practice. Wiley. ISBN: 978-1-405-16173-2.

Konishi, S., Hamacher, K., Vallabhajosula, S., Kothari, P., Bastidas, D., Bander, N., and Goldsmith, S. (2004). Determination of immunoreactive fraction of radiolabeled monoclonal antibodies: what is an appropriate method? Cancer Biother. Radiopharm. *19*, 706–715.

Kotzyba-Hilbert, F., Kapfer, I., and Goeldner, M. (1995). Recent trends in photoaffinity labeling. Angew. Chem. Int. Ed. *34*, 1296–1312.

Kumar, V., Yarravarapu, N., Lapinsky, D.J., Perley, D., Felts, B., Tomlinson, M.J., Vaughan, R.A., Henry, L.K., Lever, J.R., and Newman, A.H. (2015). Novel azido-iodo photoaffinity ligands for the human serotonin transporter based on the selective serotonin reuptake inhibitor (S)-citalopram. J. Med. Chem. *58*, 5609–5619.

Kym, P.R., Carlson, K.E., and Katzenellenbogen, J.A. (1995). Evaluation of a highly efficient aryl azide photoaffinity labeling reagent for the progesterone receptor. Bioconjug. Chem. *6*, 115–122.

Lange, C.W., VanBrocklin, H.F., and Taylor, S.E. (2002). Photoconjugation of 3-azido-5-nitrobenzyl-[18F]fluoride to an oligonucleotide aptamer. J. Label. Compd. Radiopharm. *45*, 257–268.

Lindmo, T., Boven, E., Cuttitta, F., Fedorko, J., and Bunn, P.A. (1984). Determination of the immunoreactive function of radiolabeled monoclonal antibodies by linear extrapolation to binding at infinite antigen excess. J. Immunol. Methods *72*, 77–89.

Nishikawa, M., Nakano, T., Okabe, T., Hamaguchi, N., Yamasaki, Y., Takakura, Y., Yamashita, F., and Hashida, M. (2003). Residualizing indium-111-radiolabel for plasmid DNA and its application to tissue distribution study. Bioconjug. Chem. *14*, 955–961.

Pandurangi, R.S., Karra, S.R., Katti, K.V., Kuntz, R.R., and Volkert, W.A. (1997a). Chemistry of bifunctional photoprobes. 1. perfluoroaryl azido functionalized phosphorus hydrazides as novel photoreactive heterobifunctional chelating agents: high efficiency nitrene insertion on model solvents and proteins. J. Org. Chem. *62*, 2798–2807.

Pandurangi, R.S., Lusiak, P., Kuntz, R.R., Sun, Y., and Weber, K.T. (1997c). Chemistry of bifunctional photoprobes II. chemical and photochemical modification of angiotensin converting enzyme inhibitors: implications in the development of cardiac radionuclide imaging agents. Bioorg. Chem. *87*, 77–87.

Pandurangi, R.S., Karra, S.R., Kuntzl, R.R., and Volkert, W.A. (1997b). Symposium-in-print recent trends in the evaluation of photochemical

insertion characteristics. Photochem. Photobiol. *65*, 208–221.

Pandurangi, R.S., Lusiak, P., Kuntz, R.R., Volkert, W.A., Rogowski, J., and Platz, M.S. (1998). Chemistry of bifunctional photoprobes. 3. Correlation between the efficiency of CH insertion by photolabile chelating agents and lifetimes of singlet nitrenes by flash photolysis: first example of photochemical attachment of 99mTc-complex with human serum. J. Org. Chem. *63*, 9019–9030.

Patra, M., Eichenberger, L.S., Fischer, G., and Holland, J.P. (2019). Photochemical conjugation and one-pot radiolabelling of antibodies for immuno-PET. Angew. Chem. Int. Ed. *58*, 1928–1933.

Platz, M.S. (1995). Comparison of phenylcarbene and phenylnitrene. Acc. Chem. Res. *28*, 487–492.

Rajagopalan, R., Kuntz, R.R., Sharma, U., Volkert, W.A., and Pandurangi, R.S. (2002). Chemistry of bifunctional photoprobes. 6. Synthesis and characterization of high specific activity metalated photochemical probes: development of novel rhenium photoconjugates of human serum albumin and Fab fragments. J. Org. Chem. *67*, 6748–6757.

Rylova, S.N., Del Pozzo, L., Klingeberg, C., Tonnesmann, R., Illert, A.L., Meyer, P.T., Maecke, H.R., and Holland, J.P. (2016). Immuno-PET imaging of CD30-positive lymphoma using 89Zr-desferrioxamine-labeled CD30-specific AC-10 antibody. J. Nucl. Med. *57*, 96–102.

Singh, A., Thornton, E.R., and Westheimer, F.H. (1962). The photolysis of diazo-acetylchymotrypsin. J. Biol. Chem. *237*, PC3006–PC3008.

Stalteri, M.A., and Mather, S.J. (1996). Technetium-99m labelling of the anti-tumour antibody PR1A3 by photoactivation. Eur. J. Nucl. Med. *23*, 178–187.

Sykes, T.R., Woo, T.K., Baum, R.P., Qi, P., and Noujaim, A. (1995). Direct labeling of monoclonal antibodies with technetium-99m by photoactivation. J. Nucl. Med. *36*, 1913–1922.

Sykes, T.R., Somayaji, V.A., Bier, S., Woo, T.K., Kwok, C.S., Snieckus, V., and Noujaim, A. (1997). Radiolabeling of monoclonal antibody B43.13 with rhenium-188 for immunoradiotherapy. Appl. Radiat. Isot. *48*, 899–906.

Verel, I., Visser, G.W.M., Boellaard, R., Stigter-van Walsum, M., Snow, G.B., and van Dongen, G.A.M.S. (2003a). 89Zr immuno-PET: comprehensive procedures for the production of 89Zr-labeled monoclonal antibodies. J. Nucl. Med. *44*, 1271–1281.

Verel, I., Visser, G.W.M., Boerman, O.C., van Eerd, J.E.M., Finn, R., Boellaard, R., Vosjan, M.J.W.D., Stigter-van Walsum, M., Snow, G.B., and van Dongen, G.E.M. (2003b). Long-lived positron emitters zirconium-89 and iodine-124 for scouting of therapeutic radioimmunoconjugates with PET. Cancer Biother. Radiopharm. *18*, 655–661.

Vosjan, M.J.W.D., Perk, L.R., Visser, G.W.M., Budde, M., Jurek, P., Kiefer, G.E., and van Dongen, G.A.M.S. (2010). Conjugation and radiolabeling of monoclonal antibodies with zirconium-89 for PET imaging using the bifunctional chelate p-isothiocyanatobenzyl-desferrioxamine. Nat. Protoc. *5*, 739–743.

Wester, H.J., Hamacher, K., and Stöcklin, G. (1996). A comparative study of N.C.A. fluorine-18 labeling of proteins via acylation and photochemical conjugation. Nucl. Med. Biol. *23*, 365–372.

Ziegler, T., and Rank, A. (1977). On the calculation of multiplet energies by the Hartree-Fock-slater method. Theor. Chim. Acta *43*, 261–271.

ISCI, Volume *13*

Supplemental Information

Simultaneous Photoradiochemical Labeling of Antibodies for Immuno-Positron Emission Tomography

Malay Patra, Simon Klingler, Larissa S. Eichenberger, and Jason P. Holland

Table of Contents

Transparent methods

General details

Unless otherwise stated, all chemicals were of reagent grade and purchased from SigmaAldrich (St. Louis, MO), Merck (Darmstadt, Germany), Tokyo Chemical Industry (Eschborn, Germany), abcr (Karlsruhe, Germany) or CheMatech (Dijon, France). Water (>18.2 MΩ·cm at 25 ºC, Puranity TU 3 UV/UF, VWR International, Leuven, Belgium) was used without further purification. Solvents for reactions were of reagent grade, and where necessary, were dried over molecular sieves. Evaporation of the solvents was performed under reduced pressure by using a rotary evaporator (Rotavapor R-300, Büchi Labortechnik AG, Flawil, Switzerland) at the specified temperature and pressure.

^{1}H and ^{13}C NMR spectra were measured in deuterated solvents on a Bruker AV-400 (^{1}H: 400 MHz, ^{13}C: 100.6 MHz) or a Bruker AV-500 (^{1}H: 500 MHz, ^{13}C: 125.8 MHz) spectrometer. Chemical shifts (δ) are expressed in parts per million (ppm) relative to the resonance of the residual solvent peaks, for example, with DMSO δ_H = 2.50 ppm and δ_C = 39.5 ppm with respect to tetramethylsilane (TMS, δ_H and δ_C = 0.00 ppm). Coupling constants (*J*) are reported in Hz. All resonances were assigned by using a combination of 1D and 2D NMR (HSQC, COSY) spectra. Peak multiplicities are abbreviated as follows: s (singlet), d (doublet), dd (doublet of doublets), t (triplet), q (quartet), m (multiplet), and br (broad).

High-resolution electrospray ionisation mass spectra (HR-ESI-MS) were measured by the mass spectrometry service at the Department of Chemistry, University of Zurich.

Column chromatography was performed by using Merck silica gel *60* (63 – 200 µm) with eluents indicated in the experimental section. Standard thin-layer chromatography (TLC) for synthesis employed Merck TLC plates silica gel *60* on an aluminium base with the indicated solvent system. The spots on TLC were visualised either by UV/visible light (254 nm) or by staining with $KMnO_4$.

Semi-preparative high-performance liquid chromatography (HPLC) purifications were performed using a Rigol HPLC system (Contrec AG, Dietikon, Switzerland) equipped with a C18 reverse-phase column (VP 250/21 Nucleodur C18 HTec, 21 mm ID x 250 mm, 5µm) using a flow rate of 8 mL min^{-1} with a linear gradient of solvent A (distilled H_2O containing 0.1% TFA) and B (MeOH): *t* = 0-3 min., 60% A; *t* = 25-30 min., 5% A; *t* = 33-38 min., 60% A. Electronic absorption was measured at 254 nm.

Analytical ultra-high-performance liquid chromatography (UHPLC) experiments were performed using two separate Hitachi Chromaster Ultra Rs systems fitted with either a reverse phase VP 250/4 Nucleodur C18 HTec (4 mm ID x 250 mm, 5µm) column or a reverse phase Acquity UPLC column (BEH C18, 1.7 µm, 2.1 mm ID x 50 mm). One of these systems was also connected to a radioactivity detector (FlowStar^2 LB 514, Berthold Technologies, Zug, Switzerland) equipped with a 20 µL PET cell (MX-20-6, Berthold Technologies) for analysing radiochemical reactions. Proteins were analysed by using the same UHPLC system equipped with a size-exclusion column (Enrich SEC 70 column: 24 mL volume, 10 ± 2 µm particle size, 10 mm ID x 300 mm, Bio-Rad Laboratories, Basel, Switzerland). UHPLC using the Acquity column used a flow rate of 0.6 mL min^{-1} with a linear gradient of solvent A (distilled H_2O containing 0.1% TFA) and B (acetonitrile): *t* = 0-0.5 min., 30% A; *t* = 9.5 min., 0% A; *t* = 10 min., 0% A. Electronic absorption was measured at 254 nm.

Analytical high performance liquid chromatography (HPLC) experiments for photodegradation kinetics were performed using a Hitachi Chromaster system equipped with a reverse phase column (Reproshell 100 Dr. Maisch C18, 2.8 µm, 75 x 4.6 mm) using a flow rate of 1.5 mL min^{-1} with a linear gradient of solvent A (distilled H_2O containing 0.1% HCOOH) and B (acetonitrile): *t* = 0 min., 95% A; *t* = 5.8 min., 0% A; *t* = 6.8 min., 0% A; *t* = 7.3 min., 90% A. Electronic absorption was measured at 260 nm.

Electronic absorption spectra were recorded using a Nanodrop™ One^C Microvolume UV-Vis Spectrophotometer (ThermoFisher Scientific, supplied by Witec AG, Sursee, Switzerland). Protein concentration was determined in accordance with the manufacturers protocol.

Photochemistry

Photochemical conjugation experiments were performed in transparent glass vials at the indicated concentrations. Stock solutions were prepared in H_2O (trastuzumab and DFO-ArN_3 [**1**]). Photochemical reactions were stirred gently using a magnetic stir bar. Detail procedures and reaction times are indicated in the experimental section. Irradiations used three light sources. For pre-conjugation experiments, a high-powered Rayonet reactor[1] (350 nm, 16 x 8 W Sylvania BLB-lamps, 10 cm diameter) was used. For kinetic studies and for simultaneous one-pot photoradiochemical labelling reactions, portable, high-powered, light-emitting diodes (LEDs at either 365 nm or 395 nm) were used. The LED intensity was adjusted using a UV-LED controller (Opsytec Dr. Gröbel GmbH, Ettlingen, Germany), where 100% corresponded to a power of approximately 263 mW and 355 mW for the 365 nm and 395 nm sources, respectively. LED intensity was measured using a S470C Thermal Power Sensor Head, Volume Absorber, 0.25 - 10.6 µm, 0.1mW - 5W, Ø15 mm. Total irradiance power of the Rayonet reactor was estimated to be approximately 92 mW (approximately 300 mW/cm^3). Note that calculation of exact power incident to the reaction is non-trivial because it depends on the specific geometry of the experimental set-up. The temperature of all photochemical conjugation reactions was typically 23 ± 2 °C. Emission spectra of the three light sources are shown in Figure S1. The Rayonet reactor had an experimentally measured λ_{max} at 368 nm with full-width at half-maximum (FWHM) value of 16.0 nm. The LED (365 nm) had a maximum emission intensity at 364.5 nm (FWHM of 9.1 nm). The LED (395 nm) had a maximum emission intensity at 389.9 nm (FWHM of 9.1 nm).

Figure S1, related to Figure 2. (A) Emission spectra of the Rayonet reactor (red) and the two LED light sources (365 nm, blue; 395 nm, black). (B) Measured power (mW) *versus* the digitally controlled LED intensity (%).

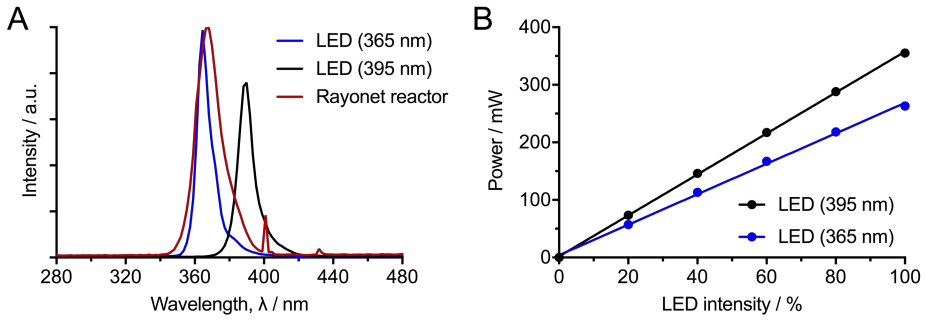

Radioactivity and radioactive measurements

All instruments for measuring radioactivity were calibrated and maintained in accordance with previously reported routine quality control procedures.[2] [^{89}Zr][Zr(C_2O_4)$_4$]$^{4-}$(aq.) was obtained as a solution in ~1.0 M oxalic acid from PerkinElmer (Boston, MA, manufactured by the BV Cyclotron VU, Amsterdam, The Netherlands) and was used without further purification. Radioactive reactions were monitored by using instant thin-layer chromatography (radio-iTLC). Glass-fibre iTLC plates impregnated with silica-gel (iTLC-SG, Agilent Technologies) were developed in using aqueous mobile phases containing either EDTA (50 mM, pH7.1) or DTPA (50 mM, pH7.4) and were analysed on a radio-TLC detector (SCAN-RAM, LabLogic Systems Ltd, Sheffield, United Kingdom). Radiochemical conversion (RCC) was determined by integrating the data obtained by the radio-TLC plate reader and determining both the percentage of radiolabelled product (R_f = 0.0) and 'free' ^{89}Zr (R_f = 1.0; present in the analyses as either [^{89}Zr]Zr(EDTA) or [^{89}Zr]Zr(DTPA). Integration and data analysis were performed by using the software Laura version 5.0.4.29 (LabLogic). Appropriate background and decay corrections were applied as necessary. Radiochemical purities (RCPs) of labelled protein samples were determined by size-exclusion chromatography (SEC) using two

different columns and techniques. The first technique used an automated size-exclusion column (Bio-Rad Laboratories, ENrich SEC 70, 10 ± 2 µm, 10 mm ID x 300 mm) connected to a UHPLC device (Hitachi ChromasterUltra Rs, VWR International, Leuven, Belgium) equipped with a UV/visible diode array detector (absorption measured at 220, 254 and/or 280 nm) as well as a radioactivity detector (FlowStar^2 LB 514, Berthold Technologies, Zug, Switzerland). Isocratic elution with phosphate buffered saline (PBS, pH7.4) was used. The second method used a manual procedure involving size-exclusion column chromatography using a PD-10 desalting column (Sephadex G-25 resin, 85-260 µm, 14.5 mm ID x 50 mm, >30 kDa, GE Healthcare). For analytical procedures, PD-10 columns were eluted with sterile saline or PBS. A total of 40 x 200 µL fractions were collected up to a final elution volume of 8 mL. Note that the loading/dead-volume of the PD-10 columns is precisely 2.50 mL which was discarded prior to aliquot collection. For quantification of radioactivity, each fraction was measured on a gamma counter (HIDEX Automatic Gamma Counter, Hidex AMG, Turku, Finland) using an energy window between 480 – 558 keV for ^{89}Zr (511 keV emission) and a counting time of 30 s. Appropriate background and decay corrections were applied throughout. PD-10 SEC columns were also used for preparative purification and reformulation of radiolabelled products by collecting a fraction of the eluate corresponding to the high molecular weight protein (>30 kDa fraction eluted in the range between 0.0 to 1.6 mL as indicated for each experiment).

Cell culture

For cell binding assays, the human ovarian cancer cell line SK-OV-3 (HER2/*neu*-positive, American Type Culture Collection [ATCC-HTB-77], Manassas, VA) was used. Cells were cultured at 37 °C in a humidified 5% CO_2 atmosphere in DMEM/F12 (1:1) (Dulbecco's Modified Eagle Medium, F-12 Nutrient mixture (Ham), ThermoFisher Scientific, Schlieren, Switzerland) medium containing [+]-L-glutamine (2.5 mM), supplemented with fetal bovine serum (FBS, 10% (v/v), ThermoFisher Scientific) and penicillin/streptomycin (P/S, 1% (v/v) of penicillin 10000 U/mL and streptomycin 10 mg/mL). Cells were grown by serial passage and were harvested by using trypsin (0.25%).

Cell binding assays (immunoreactivity)

Cell binding assays were performed in accordance with the following general procedure. SK-OV-3 cells were harvested using trypsinisation (0.25%) and collected by centrifugation (2000 RPM, 10 min.). The medium was removed and the cell pellet was resuspended in complete medium containing NaN_3 (0.1% w/w). Subsequently, a two-fold serial dilution of the number of cells was performed. Cell stocks ranging from 5 x 10^6 cells to 15 x 10^4 cells were prepared in six microcentrifuge tubes with each tube containing a final volume of 0.5 mL cell suspension. One of the four prepared dilution series was incubated with a 6000-fold molar excess of non-radiolabelled trastuzumab (98.9 µg, 0.682 nmol) with respect to [^{89}Zr]ZrDFO-azepin-trastuzumab for 1 h prior to the addition of the radiotracer as a control for accessing non-specific binding. [^{89}Zr]ZrDFO-azepin-trastuzumab formulated in sterile PBS was prepared in accordance with the procedures described below. For cell binding assays, [^{89}Zr]ZrDFO-azepin-trastuzumab (6.8 µL, 2.22 µg of protein, 0.0153 nmol, 200 kBq) was diluted with PBS (13.5 mL). A constant amount of diluted [^{89}Zr]ZrDFO-azepin-trastuzumab was added to each Eppendorf tube containing the cell suspensions (100 µL per sample, containing ~0.0164 µg of protein, 1.1 x 10^{-13} mol, ~1.5 kBq). Cells were subsequently incubated while keeping them in suspension by shaking. After 1 h at 37 °C, the Eppendorf tubes were placed on ice and the cells were pelleted by centrifugation (4 °C, 3000 RPM, 5 min.). The medium was discarded and the pellets were washed with ice cold PBS (2 x 0.5 mL, centrifugation at 4 °C, 3000 RPM, 5 min.). Important: Cells were kept on ice throughout the entire washing procedure to minimise the rate of dissociation. Subsequently, the radioactivity in each pellet was quantified with the gamma counter. Standard samples of the radiotracer (3 x 100 µL) were kept separately and served as a reference of initial radioactivity added to the cells.

The immunoreactive fraction of [^{89}Zr]ZrDFO-azepin-trastuzumab was estimated by plotting standard saturation binding curves. In addition, the immunoreactive fraction was also estimated by using procedures reported by Lindmo *et al*.[4] Linear regression analysis of a plot of (total/bound) activity *versus* (1/[number of cells]) yielded the immunoreactive fraction calculated as 1/*y*-intercept.

Stability studies

The stability of [^{89}Zr]ZrDFO-azepin-trastuzumab with respect to change in radiochemical purity due to loss of radioactivity from the protein fraction was investigated *in vitro* by incubation in human serum. Aliquots of [^{89}Zr]ZrDFO-

azepin-trastuzumab (250 µL, 81.5 µg, 0.54 nmol, 6.59 MBq, A_m ~12.1 MBq/nmol) were added to human serum (400 µL) giving a total reaction volume of 650 µL. Solutions were incubated at 37 °C and SEC-UHPLC measurements recorded at the specified time points up to 45 h. The stability was monitored by quantifying the radioactivity associated with intact [^{89}Zr]ZrDFO-azepin-trastuzumab from integration of the decay corrected SEC-UHPLC radioactive chromatograms.

Animals and xenograft models

All experiments involving mice were conducted in accordance with an animal experimentation licence approved by the Zurich Canton Veterinary Office, Switzerland (Jason P. Holland). Experimental procedures also complied with guidelines issued in the *Guide for the Care and Use of Laboratory Animals*.[5] Female athymic nude mice (Crl:NU(NCr)-*Foxn1*^{nu}, 20 – 25 g, 6 – 8 weeks old) were obtained from Charles River Laboratories Inc. (Freiburg im Breisgau, Germany), and were allowed to acclimatise at the University of Zurich Laboratory of Animal Science vivarium for at least 1 week prior to implanting tumour cells. Mice were provided with food and water *ad libitum*. Tumours were induced on the right shoulder or flank by sub-cutaneous (s.c.) injection of approx. 2.9×10^6 cells. The cells were injected in a 200 µL suspension of a 1:1 v/v mixture of PBS and reconstituted basement membrane (Corning® Matrigel® Basement Membrane Matrix, obtained from VWR International).[6] Tumours developed after a period of between 3 – 6 weeks. Tumour volume (V / mm^3) was estimated by external Vernier caliper measurements of the longest axis, a / mm, and the axis perpendicular to the longest axis, b / mm. The tumours were assumed to be spheroidal and the volume was calculated in accordance with Equation S1.

$$V = \frac{4\pi}{3} \cdot \left(\frac{a}{2}\right)^2 \cdot \left(\frac{b}{2}\right) \qquad \text{(Equation S1)}$$

Small-animal PET imaging

All mice injected with cancer cells developed tumours and the average volume of the SK-OV-3 tumours was 196 ± 74 mm^3 (n = 12 mice). Mice were randomised before the study. The tail of each mouse was warmed gently using a warm water bath immediately before administering [^{89}Zr]ZrDFO-azepin-trastuzumab (normal group n = 6 mice / group: 1.02 – 1.09 MBq, [27.5 – 29.6 µCi], 13.75 µg of protein, in 250 µL sterile PBS) *via* intravenous (i.v.) tail-vein injection (t = 0 h). Competitive inhibition studies (blocking group: n = 6 mice / group, 1.16 – 1.22 MBq, [31.4 – 33.0 µCi], 1.4 mg of total protein, in 250 µL sterile PBS) were also performed to investigate the specificity and biological activity of the radiotracer *in vivo*. Note that one mouse in the normal group was excluded from the experiment and data analysis due to an aberrant pharmacokinetic profile in which the radiolabelled antibody was rapidly extracted from circulation and accumulated almost entirely in the liver and spleen within ~8 h post-administration. Further details on this phenomenon will be reported elsewhere. Full details on radioactive dose preparation are given below. Briefly, to prepare the blocking dose, an aliquot of non-radiolabelled trastuzumab (stock solution containing 57.7 mg/mL of protein in sterile saline) was added to the [^{89}Zr]ZrDFO-azepin-trastuzumab formulation (~98-times more protein compared to the normal group).

PET imaging experiments were conducted on a Genesis G4 PET/X-ray scanner (Sofie Biosciences, Culver City, CA).[7] Approximately 5 minutes prior to recording each PET image, mice were anesthetised by inhalation of between 2 – 4% isoflurane (Attane™, Piramal Enterprises Ltd, India, supplied by Provet AG, Lyssach, Switzerland)/oxygen gas mixture and placed on the scanner bed in the prone position. PET images were recorded at various time-points between 2 h and 94 h post-administration of the radiotracer. During image acquisition, the respiration rate of the animal was monitored via live video feed and anaesthesia was maintained by an experience animal experimenter by controlling the isoflurane dose between 1.5 – 2.0%. List-mode data were acquired for 10 min. using a γ-ray energy window of 150–650 keV, and a coincidence timing window of 20 ns. Images were reconstructed by iterative ordered subset maximum expectation (OSEM; 60 iterations) protocols. The reported reconstructed spatial resolution is 2.4 µL at the centre of the field-of-view (FOV). Image data were normalised to correct for non-uniformity of response of the PET, attenuation, random events, dead-time count losses, positron branching ratio, and physical decay to the time of injection, but no scatter or partial-volume averaging correction was applied. An empirically determined system calibration factor (in units of [Bq/voxel]/[MBq/g] or [Bq/cm^3]/[MBq/g]) for mice was used to convert voxel count rates to

activity concentrations. The resulting image data were normalised to the administered activity to parameterise images in terms of %ID/cm^3 (equivalent to units of %ID/g assuming a tissue density of unity). Images were analysed by using VivoQuant^{TM} 3.5 patch 2 software (InviCRO, Boston, MA). For image quantification and measurements of time-activity curves (TACs), 3-dimensional volumes-of-interest (VOIs) were drawn manually to determine the maximum and mean accumulation of radioactivity (in units of %ID/cm^3 and decay corrected to the time of injection) in various tissues. Where appropriate, data were also converted into mean standardised uptake values (SUV_{mean}).

Biodistribution studies

Biodistribution studies were conducted after the final imaging time point to evaluate the radiotracer uptake in tumour-bearing mice. Animals (n = 6 mice / group) were anaesthetised individually by isoflurane and euthanised by isoflurane asphyxiation followed by terminal exsanguination. Note: one mouse was excluded from the analysis of the data from the normal group (*vide supra*). A total of 15 tissues (including the tumour) were removed, rinsed in water, dried in air for approx. 2 min., weighed and counted on a calibrated gamma counter for accumulation of activity. The mass of radiotracer formulation injected into each animal was measured and used to determine the total number of counts per minute (cpm) injected into each mouse by comparison to a standard syringe of known activity and mass. Count data were background- and decay-corrected, and the tissue uptake for each sample (determined in units of percentage injected dose per gram [%ID/g]) was calculated by normalisation to the total amount of activity injected for each individual animal. For comparison purposes, data are also presented in terms of SUV.

Effective half-life, $t_{1/2}$(eff)

The effective half-life $t_{1/2}$(eff) of [^{89}Zr]ZrDFO-azepin-trastuzumab was measured in the same athymic nude mice used for small-animal PET imaging and end time point biodistribution. Total internal radioactivity was measured as a function of time by using a dose calibrator.

Computational details

All calculations were conducted using density functional theory (DFT) as implemented in the Gaussian16 Revision A.03 suite of *ab initio* quantum chemistry programs. Normal self-consistent field (SCF) and geometry convergence criteria were employed throughout. All structures were optimised in the gas phase and in solution phase using a polarisable continuum model (PCM). With the exception of calculations on the arylnitrene (ArN) intermediate which were calculated using C_{2v} symmetry, all other structures were optimised without using symmetry constraints. Solvated phase calculations were implemented using the SCRF keyword with default parameters and selecting water as the solvent (dielectric constant, ε = 78.3553). Harmonic frequency analysis based on analytical second derivative was used to characterise optimised structures as local minima or first order saddle points (transition states) on the potential energy surface. Calculations were performed using the unrestricted uB3LYP exchange-correlation functionals and the triple-ζ 6-311++G(d,p) basis set by Pople and co-workers. The choice of solvation model reflects our standard aqueous phase conditions employed in the photoradiochemical synthesis of [^{89}Zr]ZrDFO-azepin-trastuzumab. Optimised structures and molecular orbitals were analysed by using Chemcraft (version 1.8, build 536b).

For closed shell singlet species, the calculations converged to the restricted result. Calculations on the arylnitrene species (C_{2v} symmetry) in the open-shell singlet ($^1A_2$ state) or triplet ($^3A_2$ state) required the unrestricted formalism. Ground state geometry optimisations of arylazide (ArN) specifying the singlet state converged to the higher energy $^1A_1$ state with a $(p_y)^2$ electronic configuration where both electrons occupied the in-plane p_y orbital. Checks on the stability of the wavefunction confirmed that this state was unstable with respect to both the lower energy open-shell $^1A_2$ state $(p_x)^1(p_y)^1$ configuration and also the lower energy $^3A_2$ state. Geometry optimisation of ArN in the triplet state was accomplished by specifying the triple state in the root section. Optimisation to the lowest energy open-shell singlet $^1A_2$ state required control over the molecular orbital population using the Guess=(always,alter) keyword. The initial orbital population guess placed both the alpha and beta electrons in the highest occupied molecular orbitals (HOMOs) which had B_2 symmetry and corresponding to the in-plane p_y orbital on the N atom. In both the alpha and beta orbital manifolds the lowest unoccupied molecular orbital (LUMO) had B_1 symmetry and corresponded to the to the out-of-plane p_x orbital on the N atom. Convergence to the $^1A_2$ state was achieved by switching the orbital occupancy from the 24(B_2) orbital to the 25(B_1) orbital in the beta manifold. Note that spin contamination was observed in the optimised $^1A_2$ state calculations with the spin expectation value of <S2> = 1.000 indicating a 50:50 mixture with a triplet contamination. Therefore, energies of the $^1A_2$ state were estimated using the sum method reported by Ziegler *et al*.[3] The structure of the alternative higher energy closed-shell $^1A_1$ singlet state with a $(p_x)^2$ electronic configuration was also optimised using a similar control of the orbital populations.

Time-dependent density functional theory (TD-DFT) calculations were performed on the model compound arylazide (PhN_3). Transition energies and oscillator strengths for electronic excitation to the first 16 excited states (including both singlet and triplet states) were calculated by using the unrestricted uB3LYP/6-311++G(d,p) methodology incorporating the default PCM in water. No symmetry constraints were used in TD-DFT calculations. The simulated TD-DFT electronic absorption spectrum in Figure 4 (main article) was calculated by using a Lorentzian line broadening function with a full-width at half maximum (FWHM) value set at 20 nm (implemented in Chemcraft). Absolute calculated transition energies were shifted linearly by Δ = +12 nm to optimise the overlay with the experimental spectrum but scaling factors were not used.

Table S1, related to Figures 4 and 5. Calculated electronic excitation transition energies and oscillator strengths based on the TD-DFT calculation (uB3LYP/6-311++G(d,p)/PCM) of the first 16 excited states (singlets and triplets) of the model compound arylazide (PhN_3).

Band label (singlet states only)	Calculated transition energy / nm[a]	Calculated oscillator strength, *f* / a.u.	Excited state spin state	Assignment and molecular orbital contributions (%)
	395.3	0	Triplet	
	371.43	0	Triplet	
A	337.75	0.0003	Singlet	HOMO → LUMO (96.4%)
	311.45	0	Triplet	
	299.84	0	Triplet	
	275.26	0	Triplet	
B	272.54	0.1958	Singlet	HOMO → LUMO+2 (66.3%) HOMO → LUMO+3 (20.0%)
	269	0	Triplet	
C	262.64	0.1656	Singlet	HOMO → LUMO+3 (48.3%) HOMO → LUMO+2 (24.9%) HOMO-1 → LUMO+1 (23.7%)
	259.5	0	Triplet	
	250.8	0	Triplet	
D	250.45	0.0001	Singlet	
	231.21	0	Triplet	
E	229.49	0.0001	Singlet	
	225.72	0	Triplet	
F	224.14	0.2481	Singlet	HOMO-1 → LUMO+2 (66.7%) HOMO → LUMO+3 (30.3%)

[a] Note that all calculated energies are *x*-shifted by Δ = +12 nm for clarity with overlay of the TD-DFT calculated spectrum of the model compound arylazide (PhN^3) and the experimental electronic absorption spectrum of compound **1**.

Statistical analysis

Where appropriate, data were analysed by the unpaired, two-tailed Student's *t*-test. Differences at the 95% confidence level (*P*-value <0.05) were considered to be statistically significant.

Synthesis and chemical characterisation

Chemical syntheses were performed in accordance with Scheme 2 (main article). All reactions involving photosensitive compounds were performed in the dark. Herceptin™ was generously provided by Genentech (South San Francisco, CA) and was initially reconstituted in water. The IgG_1 antibody component (trastuzumab) was purified from Herceptin™ by spin column centrifugation (4000 RPM, 3 x 15 min., 1 x 20 min.) by using a membrane filter (Amicon Ultra-4 mL centrifugal filter, Millipore, 10 kDa MWCO). Briefly, aliquots of Herceptin™ (60 mg) were washed with H_2O (4 x 4 mL) at room temperature and concentrated before use. After concentration, protein samples were removed from the centrifugation filter by rinsing with water (500 μL) and the protein concentration was determined using a Nanodrop™ One^C Microvolume UV-Vis Spectrophotometer. Typically, 25 – 30 mg of protein was obtained and samples were aliquoted into Eppendorf tubes and stored at -20 ºC for future use.

Synthesis of desferrioxamine-*p*-arylazide, DFO-ArN_3 (**1**)

A solution of 4-azidobenzoic acid (206 mg, 1.26 mmol), HATU (506 mg, 1.33 mmol) and *N,N*-diisopropylethylamine (DIPEA, 130 μL) in dry DMF (8 mL) was stirred at room temperature for 40 min. Then desferrioxamine B mesylate (DFO, 407 mg, 0.725 mmol) was added to the mixture along with additional DIPEA (95 μL) and *N*-methylmorpholine (250 μL). After stirring at room temperature for 80 h, the mixture was transferred to a single-necked round bottom flask (100 mL) and the solvent was evaporated under reduced pressure (25 mbar). The orange-beige residue was washed by sonication with cold acetone (6 x 7 mL, -20 °C) and ice-cold H_2O (4 x 7 mL). Note that between each washing step, the solid residue was collected by centrifugation and cooled. Washing with acetone the orange colour and subsequent lyophilisation gave the crude product DFO-ArN_3 (**1**, 40% yield, 228 mg, 0.291 mmol, estimated 68% purity measured by ^{1}H NMR) as a white amorphous powder. A portion of the crude product was purified by semi-preparative HPLC and after lyophilisation, purified compound **1** was obtained as a white amorphous powder. (Yield 4%, estimated purity >95% by UHPLC and by ^{1}H NMR). ^{1}H NMR (DMSO-d_6; 500 MHz): δ (ppm) 9.64 – 9.59 (3H, m, 3 x N-OH); 8.44 (1H, t, *J* = 5.4, NHCOPh); 7.88 (2H, arom. d, *J* = 8.8); 7.77 (2H, m, 2 x NH); 7.19 (2H, arom. d, *J* = 8.8); 3.48 – 3.44 (6H, m, 3 x CONOHC*H*$_2$); 3.24 – 3.20 (2H, m, PhCONHC*H*$_2$); 3.00 – 2.98 (4H, m, 2 x CH_2CONHC*H*$_2$); 2.57 (4H, t, *J* = 6.9, 2 x NHCOCH_2C*H*$_2$CONOH); 2.26 (4H, t, *J* = 7.1, 2 x NHCOC*H*$_2$$CH_2$CONOH); 1.96 (3H, s, CH_3); 1.54 – 1.49 (8H, m, 4 x CH_2, 3 x CONOHCH$_2$C*H*$_2$$CH_2$$CH_2$$CH_2$NHCO + PhCONHCH$_2$C*H*$_2$); 1.39 – 1.35 (4H, m, 2 x CH_2CONHCH$_2$C*H*$_2$); 1.28 – 1.21 (6H, m, 3 x CONOHCH$_2$$CH_2$C*H*$_2$$CH_2$$CH_2$NHCO). ^{13}C{^{1}H} NMR (DMSO-d_6; 125.8 MHz): δ (ppm) 172.0, 171.3, 170.1, 165.1 (6 CO); 142.1, 131.3 (2C, arom.); 129.0, 118.8 (4C, arom., 4 x CH); 47.1, 46.8 (3C, 3 x CONOH*C*H$_2$); 39.1 (1C, PhCONH*C*H$_2$, signal overlaps with solvent signal); 38.4 (2C, 2 x CH_2CONH*C*H$_2$); 29.9 (2C, 2 x NHCO*C*H$_2$$CH_2$CONOH); 28.8 (CONOHCH$_2$*C*H$_2$$CH_2$*C*H$_2$$CH_2$NHCO + PhCONHCH$_2$*C*H$_2$); 27.6 (2C, 2 x NHCOCH$_2$C*H*$_2$CONOH); 26.0 (CONOHCH$_2$*C*H$_2$$CH_2$$CH_2$$CH_2$NHCO + PhCONHCH$_2$*C*H$_2$); 23.6, 23.5 (3C, 3 x CONOHCH$_2$$CH_2$C*H*$_2$$CH_2$$CH_2$NHCO); 20.4 (1C, CH_3). UV/vis (MeOH): λ_{max} 269 nm (ε = 72,400 M^{-1} cm^{-1}). HR-ESI(+)-MS (MeOH): *m/z* calc. for [M + Na^+] 728.37020, found 728.36983 (100%, Δ = -0.51 ppm). t_R (RP-UHPLC) = 3.30 min (detection at λ = 254 nm). RP-UHPLC method: A flow rate of 0.6 mL min^{-1} with a linear gradient of A (distilled H_2O containing 0.1% TFA) and B (acetonitrile): *t* = 0-0.5 min, 70% A; *t* = 9.5-10 min, 0% A.

Figure S2, related to Scheme 2. HR-ESI-MS data for DFO-ArN_3 (**1**), *m*/*z* $[M+Na]^+$ = 728.36983 (100%).

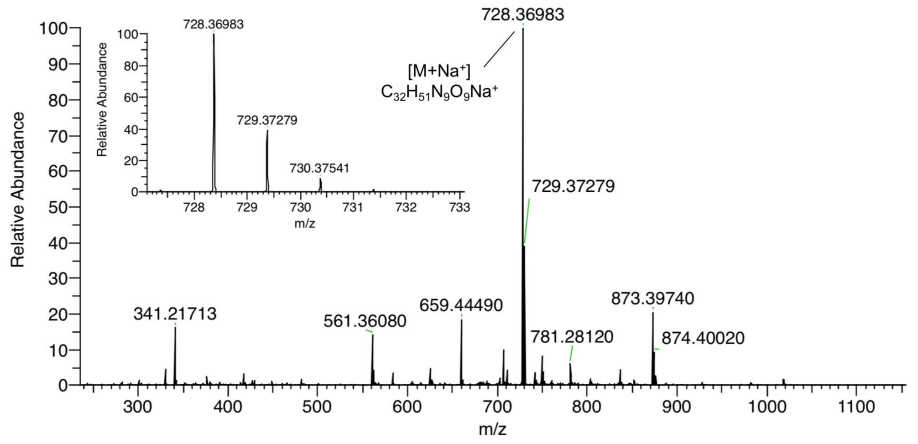

Rank	Peak Mass	Theo. mass	Display Formula	Delta [ppm]	RDB	Combined Fit
1	728.36983	728.37020	$C_{32}H_{51}O_9N_9{}^{23}Na$	-0.51	11.50	76.3110925763315

Figure S3, related to Scheme 2. Reverse-phase UHPLC chromatogram of compound **1** (λ = 254 nm).

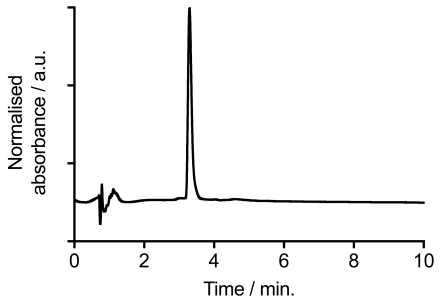

Figure S4, related to Scheme 2. ^{1}H NMR spectrum (DMSO-d_6, 500 MHz) of compound **1**.

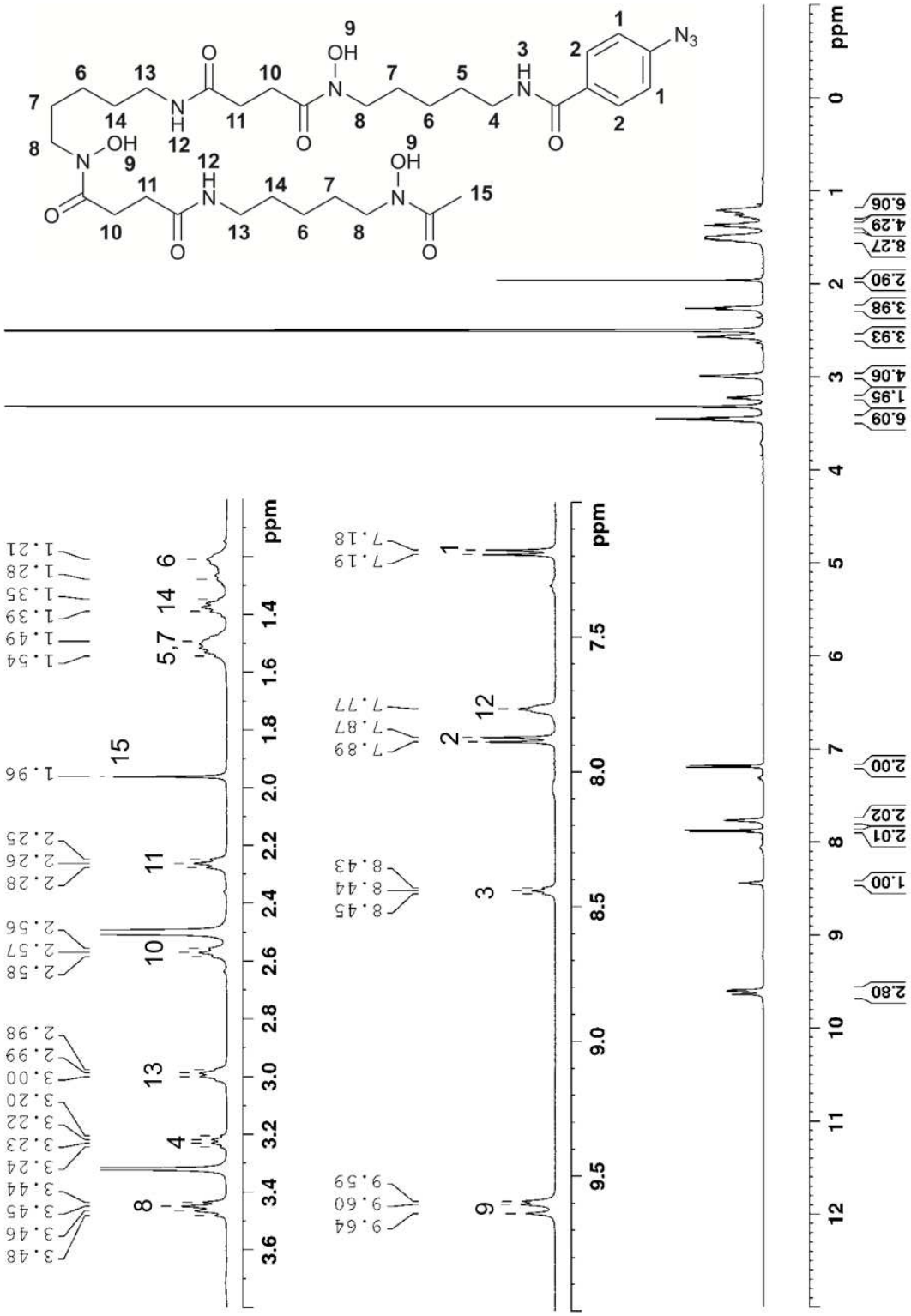

Figure S5, related to Scheme 2. $^{13}C\{^{1}H\}$ NMR spectrum (DMSO-d_6, 125.8 MHz) of compound **1**.

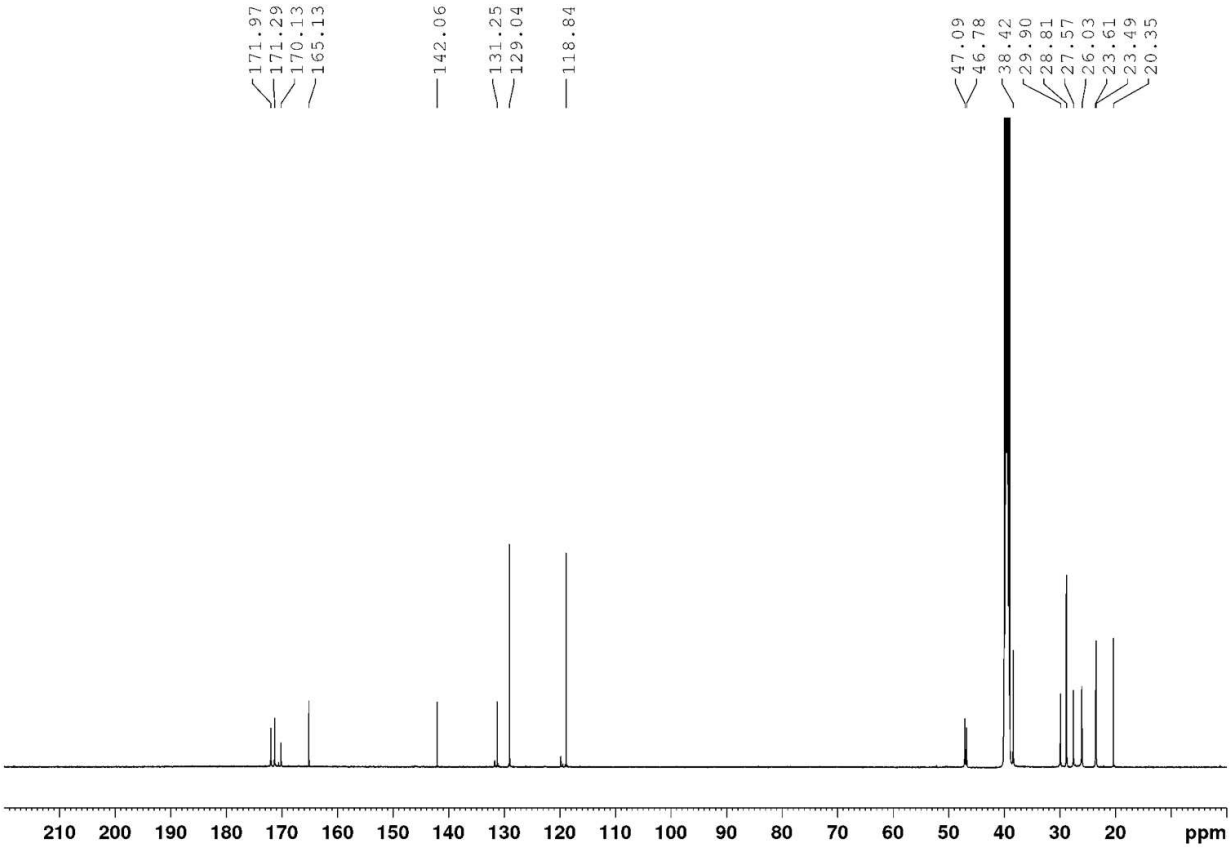

Figure S6, related to Scheme 2. COSY spectrum (DMSO-d_6, 500 MHz) of compound **1**.

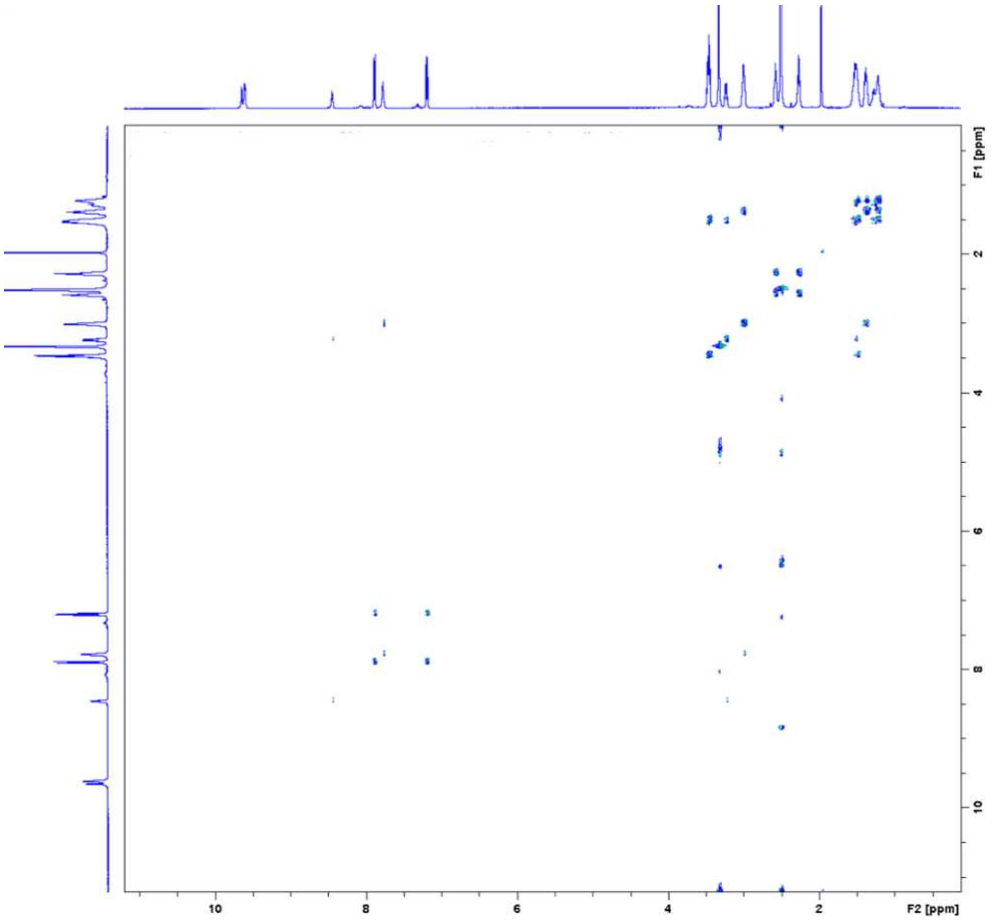

Figure S7, related to Scheme 2. HSQC spectrum (DMSO-d_6) of compound **1**.

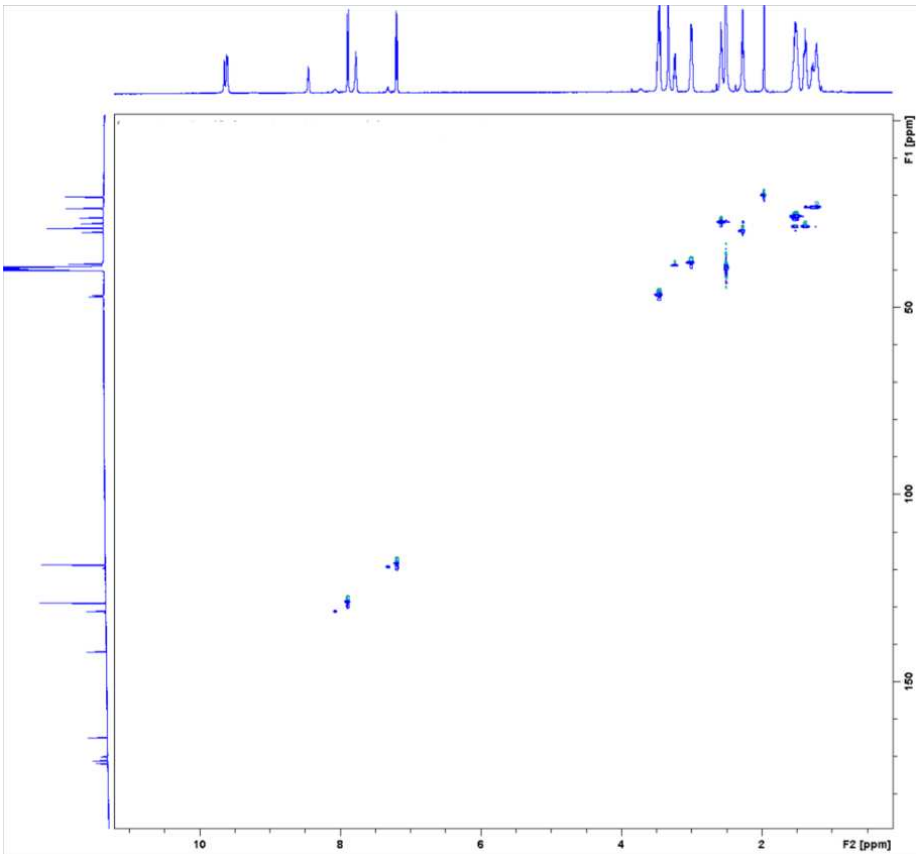

Figure S8, related to Scheme 2. (A) Experimental electronic absorption spectrum of DFO-ArN_3 (**1**). (B) Plot of the measured molar absorption coefficients of compound **1** at 365 nm (blue) and 395 nm (black).

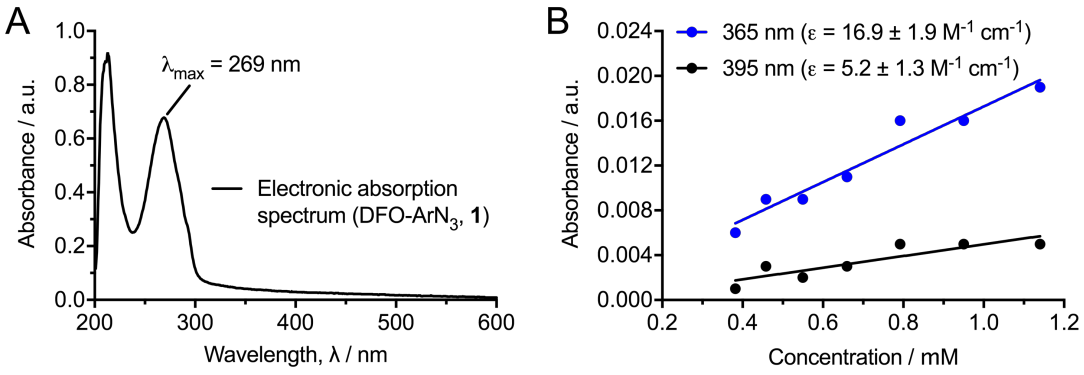

Synthesis of $[ZrDFO\text{-}ArN_3]^+$ (Zr-**1**$^+$)

DFO-ArN_3 (**1**, 0.68 mg, 0.964 μmol) was dissolved in a mixture of H_2O (50 μL) and NaOH(aq.) (0.1 M, 30 μL). After dissolution of compound **1**, a clear, colourless solution was obtained. Then the pH of the mixture was reduced to ~8 – 9 by the addition HCl(aq.) (0.1 M, 2 x 10 μL). Then an aliquot of $ZrCl_4$(aq.) (112 μL, 6 M Zr^{4+} ions dissolved in 0.1 M HCl(aq.)) was added dropwise. The reaction was monitored by RP-UHPLC and after stirring at room temperature for 2 h, complete conversion was observed. Presence of desired product Zr-**1**$^+$ was confirmed by a single peak in analytical HPLC that gave the expected mass of molecular ion as the base peak in high-resolution electrospray ionisation mass spectrometry (see Figure 1 main article and Figure S9 below). t_R (RP-HPLC) = 9.47 min (detection at λ = 254 nm). RP-HPLC method: A flow rate of 0.7 mL min^{-1} with a linear gradient of A (distilled H_2O containing 0.1% TFA) and B (acetonitrile): *t* = 0 min, 90% A; *t* = 20 min, 10% A. HR-ESI(+)-MS (MeOH): *m/z* calc. for [M^+] 792.262165, found 792.26200 (100%, Δ = 0.43 ppm).

Figure S9, related to Figure 1. Reverse-phase HPLC chromatogram of compound Zr-**1**$^+$ (λ = 254 nm).

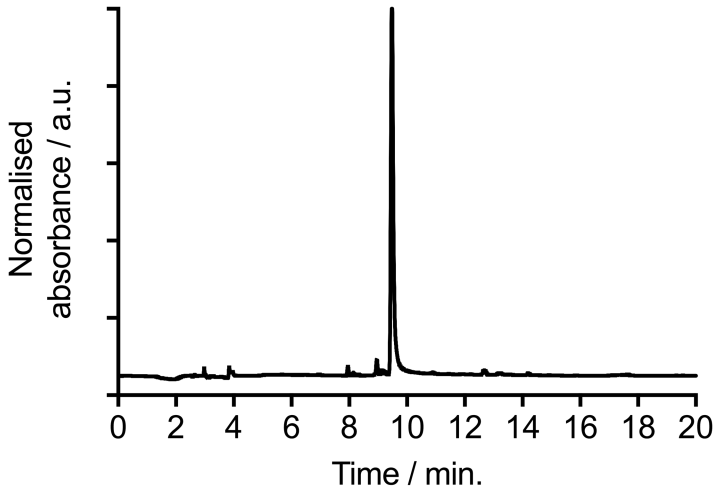

Figure S10, related to Figure 1. HR-ESI-MS data for $[ZrDFO\text{-}ArN_3]^+$ (Zr-**1**$^+$), *m*/*z* $[M^+]$ = 792.26200 (100%).

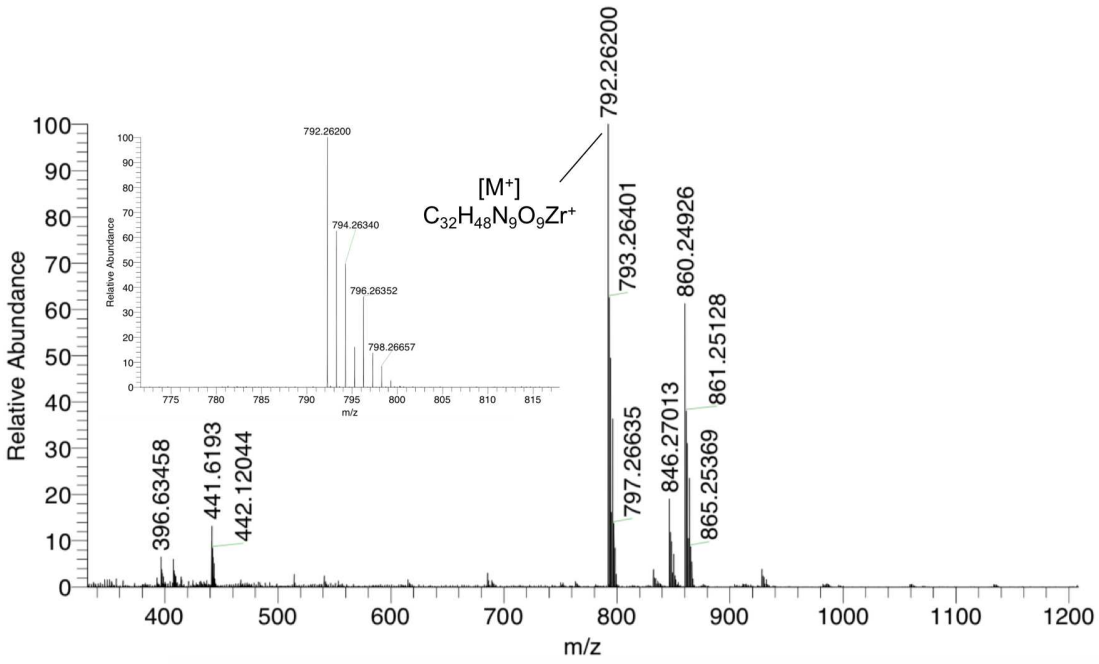

Photochemical reaction kinetics

DFO-ArN_3 (**1**, 0.31 mg, 0.44 μmol) was dissolved in H_2O (266 μL) and NaOH(aq.) (21 μL of a 0.1 M stock solution) in a transparent reaction vial equipped with a magnetic stir bar. Immediately before starting the photochemical conjugation reactions, the pH of the DFO-ArN_3 solution was reduced to ~8 – 9 by the addition of HCl(aq.) (12.6 μL of a 0.1 M stock solution). The sample was irradiated directly from above with a sheet of white paper placed between the vial and the stirring plate. The reactions (performed in duplicate) were irradiated at the specified LED intensity and aliquots (30 μL) were removed at the given time points and analysed by electronic absorption UHPLC. Photochemical degradation kinetic data are presented in Figure 2 (main article) and Table S2.

Table S2, related to Figure 2. Experimental data on the change in the relative concentration of [ZrDFO-ArN_3]$^+$ (Zr-**1**$^+$) during irradiation at 365 nm with the specified LED intensity.

Time / min.	LED intensity (100%)		LED intensity (50%)		LED intensity (20%)	
	Sample A	Sample B	Sample A	Sample B	Sample A	Sample B
0	1.0	1.0	1.0	1.0	1.0	1.0
2	0.308	0.345				
4	0.129	0.121	0.413	0.363		
6	0.040	0.061				
8	0.030	0.034	0.140	0.135	0.320	0.301
10	0.026	0.028				
12			0.061	0.076		
16			0.033	0.043	0.103	0.087
20			0.028	0.038		
24					0.056	0.029
32					0.032	0.021
40					0.028	0.019

Radiochemistry and photoradiochemistry

Molar activity of the $[^{89}Zr][Zr(C_2O_4)_4]^{4-}$(aq.) stock solution

The molar activity of the ^{89}Zr-oxalate stock solution was measured by isotopic dilution assays. Briefly, a stock solution of desferrioxamine B mesylate was prepared in water (3.77 mg, MW = 656.79 g mol^{-1}, 5.74 μmol, 1.0 mL, [DFO] = 5.74 mM) and was diluted to give a secondary solution (2.87 μM). To microcentrifuge tubes (n = 3) was added H_2O (90 μL) and an aliquot of the secondary DFO stock solution (10 μL, 0.0287 nmol). Then an aliquot of a neutralised $[^{89}Zr][Zr(C_2O_4)_4]^{4-}$(aq.) stock solution (see below for details on the neutralisation step) was added to each tube (~1.637 MBq). Reactions were vortexed and incubated at room temperature for 90 min. to ensure complete reaction occurred. At the end of the reaction, aliquots were spotted onto iTLC plates and developed using aqueous mobile phase containing DTPA (50 mM, pH7.4) or EDTA (50 mM, pH7.1). Radio-iTLC analysis was used to measure the radiochemical conversion (RCC) with the product $[^{89}Zr]$ZrDFO retained at the baseline (R_f = 0.0) and either $[^{89}Zr]$Zr(EDTA) or $[^{89}Zr]$Zr(DTPA) eluting at the solvent front (R_f = 1.0). The experimentally measured molar activity of the $[^{89}Zr][Zr(C_2O_4)_4]^{4-}$(aq.) stock solution was A_m = 37.0 ± 0.12 MBq/nmol.

Radiosynthesis and characterisation of $[^{89}Zr][ZrDFO\text{-}ArN_3]^+$ (^{89}Zr-**1**$^+$)

A stock solution of DFO-ArN_3 (**1**, 0.67 mg, 0.950 μmol) was dissolved in H_2O (50 μL) and NaOH(aq.) (30 μL of a 0.1 M stock solution). The pH of the DFO-ArN_3 solution was reduced to ~8 – 9 by the addition of HCl(aq.) (2 x 10 μL of a 0.1 M stock solution). A stock solution of $[^{89}Zr][Zr(C_2O_4)_4]^{4-}$ was prepared by adding ^{89}Zr radioactivity from the source (68.7 MBq, 70 μL in ~1.0 M aqueous oxalic acid) to a vial containing water (200 μL). The solution was neutralised and made slightly basic by the addition of aliquots of Na_2CO_3(aq.) (1.0 M stock solution, 55 μL added, final pH ~8.3 – 8.5). Caution: Acid neutralisation with Na_2CO_3 releases CO_2(g) and care should be taken to ensure that no radioactivity escapes the microcentrifuge tube. After CO_2 evolution ceased, an aliquot of the neutralised $[^{89}Zr][Zr(C_2O_4)_4]^{4-}$ solution (20 – 40 μL, 4.66 MBq) was added to the reaction microcentrifuge vial containing an aliquot of the DFO-ArN_3 stock solution (10 μL, 95 nmol, 9.5 mM) and water (50 μL) giving a clear, colourless solution (pH 7 – 8). The reaction was vortexed and incubated at room temperature. Reaction progress was monitored by radio-ITLC and complete radiochemical conversion to give of ^{89}Zr-**1**$^+$ (R_f = 0.0) was observed in <10 min. Aliquots of the crude reaction mixture were analysed be radioactive HPLC (Figure 1, main text). A single peak was observed in the radioactive trace. The identity of the radiolabelled compound ^{89}Zr-**1**$^+$ was confirmed by co-injection with an authenticated sample of ^{nat}Zr-**1**$^+$. t_R (RP-HPLC) = 9.48 min. (detection at λ = 220, 254 and 280 nm, Figure 1, main text). RP-HPLC method: A flow rate of 0.7 mL min^{-1} with a linear gradient of A (distilled H_2O containing 0.1% TFA) and B (acetonitrile): t = 0 min, 90% A; t = 20 min, 10% A.

Photochemical conjugation

General procedure for photochemical conjugation: A stock solution of photoactive ligand was prepared by dissolving DFO-ArN_3 (**1**, 0.85 mg, 1.21 μmol) in water (50 μL) and NaOH(aq.) (40 μL of a 0.1 M stock solution). Immediately before starting the photochemical conjugation reactions, the pH of the DFO-ArN_3 solution was reduced to ~9 by the addition of HCl(aq.) (2 x 10 μL of a 0.1 M stock solution). Note: DFO-ArN_3 (**1**) is sparingly soluble at high pH but starts to precipitate slowly when the pH decreases below ~9. For this reason, photochemical reactions should be initiated immediately after adding the HCl and the protein. After adjusting the pH, aliquots of the DFO-ArN_3 stock solution were added to clear 2 mL glass vials equipped with small magnetic stirring bars and containing an aqueous solution of trastuzumab (120 μL, 2.76 mg, 1.84 x 10^{-8} mol, stock protein concentration = 23.0 mg/mL) and a variable amount of water (constant total reaction volume = 200 μL). The chelate-to-mAb ratio was varied used 5.3-fold (9 μL), 10.7-fold (18 μL) or 26.4-fold (45 μL) excess of DFO-ArN_3 stock solution. The final pH of the solutions was 8-8.5. The reaction mixture was then irradiated for 25 min. using the Rayonet reactor. The irradiated crude mixture was then purified by a three-step procedure. First, the mixture was taken in a 30 kDa MWCO membrane centrifugal filter (Amicon Ultra-4 mL centrifugal filter, Millipore,), concentrated and washed with PBS (2 x 4 mL) using centrifugation (4000 RPM, ~15 min). Then the mixture was purified using a preparative PD-10-SEC column (eluted with PBS, collecting the 0.0 – 1.6 mL fraction immediately after discarding the 2.5 mL column dead volume). In the last step, the

fraction from PD-10-SEC was taken in a new 30 kDa MWCO membrane centrifugal filter, washed and concentrated using PBS (2 x 4 mL) followed by water (2 x 4 mL) as described in first step. The purified protein was removed from the spin column filter in a final volume of ~320 μL water. Protein concentration was measured using the Nanodrop. Stock solutions of DFO-azepin-trastuzumab were aliquoted and stored at -20 °C.

^{89}Zr-radiolabelling of DFO-azepin-trastuzumab

For animal experiments, the radiochemical synthesis of [^{89}Zr]ZrDFO-azepin-trastuzumab was scaled up using a sample of DFO-azepin-trastuzumab prepared from an initial chelate-to-antibody ratio of 26.4-to-1 in the photochemical conjugation reaction. To a microcentrifuge tube was added water (100 μL) and [^{89}Zr][Zr(C_2O_4)$_4$]$^{4-}$(aq.) stock solution (70 μL, 88.66 MBq). The oxalic acid was neutralised and made slightly basic by the addition of aliquots of Na_2CO_3(aq.) (~1.0 M, 55 μL, final pH8.1 – 8.3). Caution: Acid neutralisation with Na_2CO_3 releases CO_2(g) and care should be taken to ensure that no radioactivity escapes the microcentrifuge tube. After CO_2 evolution ceased, an aliquot of photochemically conjugated DFO-azepin-trastuzumab (125 μL, 8.0 mg/mL, mass = 1.0 mg of protein, 6.67 nmol) produced using an initial chelate-to-mAb ratio of 26.4-to-1 was added to the neutralised solution of [^{89}Zr][Zr(C_2O_4)$_4$]$^{4-}$(aq.). The pH decreased slightly to 6.6 and was readjusted to pH7.4 – 7.7 by the addition of Na_2CO_3(aq.) (~1.0 M, 4 μL). The reaction was mixed gently and then incubated at room temperature for 1 h. The reaction was monitored by radio-iTLC. Control reactions performed in the absence of antibody showed complete formation of [^{89}Zr]Zr(EDTA) under the conditions used to develop the iTLC plates with no activity retained at the baseline (R_f = 0.0). The reaction showed a RCC >95% after the 15 minutes but a slight improvement in RCC occurred by 40 min. (RCC >98%), which remained the same by 60 min. After 1 h, the reaction was quenched by the addition of a small aliquot of EDTA (5 μL, 50 mM, pH7.4) and incubating for a further 5 min. An aliquot of the crude mixture was retained for further analysis and then the major fraction (250 μL) was purified by preparative PD-10-SEC eluting with sterile PBS. All crude and purified mixtures were analysed by radio-iTLC, analytical PD-10-SEC and SEC-UHPLC.

The radiochemical purity (RCP) of the crude sample of [^{89}Zr]ZrDFO-azepin-trastuzumab was determined by analytical PD-10-SEC (>98%) as well as SEC-HPLC (>98%). Purification and formulation [^{89}Zr]ZrDFO-azepin-trastuzumab (pH7.4) was completed in <5 min. with a decay corrected radiochemical yield (RCY) of >99%, and a final activity concentration of 29.67 MBq/mL. After preparative PD-10-SEC (collecting the 0.0 – 1.8 mL fraction) the RCP was to >99.5% (measured by analytical PD-10-SEC) and >98% (measured by SEC-UHPLC).

Aliquots of the final [^{89}Zr]ZrDFO-azepin-trastuzumab product were then prepared for injection in the normal and blocking groups of animals (n = 6 mice / group). Briefly, two aliquots of [^{89}Zr]ZrDFO-azepin-trastuzumab (350 μL, ~10.4 MBq) were added to separate centrifuge tubes. For the normal group dose, the activity was diluted with sterile PBS (1.65 mL) giving a final volume of 2.0 mL. For the blocking group, the activity was diluted with sterile PBS (1.511 mL) and then an aliquot of non-radiolabelled trastuzumab (stock protein concentration = 57.7 mg/mL, 0.139 mL, 8.0 mg) was added and the solution mixed gently. A total of 7 syringes (250 μL/each) were drawn for both the normal and blocking formulations. The seventh syringe was used as a standard for accurate quantification of the biodistribution data (*vide supra*). In addition, aliquots of the normal and blocking formulations were retained and the protein concentration was re-measured using the Nanodrop. The measured molar activities (A_m / [MBq/nmol] of protein) of the injectates (decay-corrected to the point of final formulation) were then calculated as 13.7 MBq/nmol for the normal doses and 0.14 MBq/nmol for the blocking doses. The blocking dose contained ~98-fold higher concentration of mAb than the normal dose.

Chelate number estimation

The number of chemically accessible chelates per antibody produced after photochemically conjugating trastuzumab with different initial chelate-to-antibody ratios were estimated by radiolabelling the DFO-azepin-trastuzumab samples using an excess of [^{89}Zr][Zr(C_2O_4)$_4$]$^{4-}$(aq.), ensuring that the RCC was < 100%. Samples of the crude radiolabelling reactions forming [^{89}Zr]ZrDFO-azepin-trastuzumab were analysed by radio-ITLC eluting with EDTA. The fraction of ^{89}Zr radioactivity retained at the baseline (R_f = 0.0) and at the solvent front (R_f = 1.0, [^{89}Zr]ZrEDTA) was determined by integration after appropriate background corrections. Radio-ITLC data for the reaction using the 26.4-fold initial chelate-to-mAb ratio is shown in Figure 7A and a plot of the RCC / % *versus* time for reactions using different initial chelate-to-mAb ratios is presented in Figure 7B. Equivalent radio-ITLC data for reactions using 5.3-fold and 10-7-fold

initial chelate-to-mAb ratios are given in Figure S11A and S11B. After allowing sufficient time for saturation of the accessible chelates (180 min.), the final RCC was used to estimate the number of accessible chelates per antibody using the measured (decay corrected) molar activity of $[^{89}Zr][Zr(C_2O_4)_4]^{4-}$ and the known number of moles of antibody added to each reaction. Note that it was assumed that Zr^{4+} ions form a 1:1 stoichiometric complex with DFO (Figure S11C). The measured accessible chelate-to-mAb ratios were 0.27, 0.55 and 0.85 for DFO-azepin-trastuzumab samples prepared at initial chelate-to-mAb ratios of 5.3, 10.7 and 26.4, respectively. Linear regression analysis indicated that the quantum yield for photochemical coupling of compound **1** with trastuzumab was ~0.035. The relatively low efficiency is likely due to intramolecular reactions between the activated nitrene, benzazirine or ketenimines intermediates are nucleophilic groups (like hydroxamate anions) in the structure of DFO. See the main text for further discussions about the quantum yield and photochemical conjugation efficiency using ^{89}Zr-**1**$^{+}$.

Figure S11, related to Figure 7. Radio-ITLC data showing the change in radiochemical conversion *versus* time for the radiosynthesis of $[^{89}Zr]$ZrDFO-azepin-trastuzumab using pre-photochemically conjugated DFO-azepin-trastuzumab samples prepared with an initial chelate-to-mAb ratio of (A) 5.3-fold, and (B) 10.7-fold. (C) Plot of the experimentally determined accessible chelate-to-mAb ratio *versus* the initial chelate-to-mAb ratio used in the photochemical conjugation step.

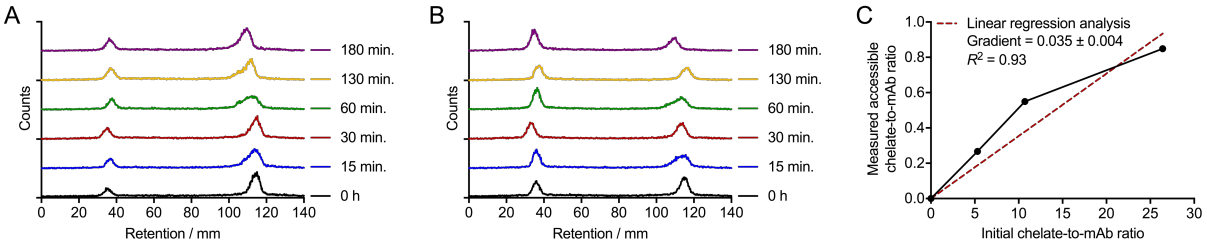

PET imaging

Figure S12, related to Figure 9. Temporal [^{89}Zr]ZrDFO-azepin-trastuzumab (normal group) PET images recorded a mouse bearing SK-OV-3 tumours on the right flank. T = tumour, H = heart, L = liver, Sp = spleen.

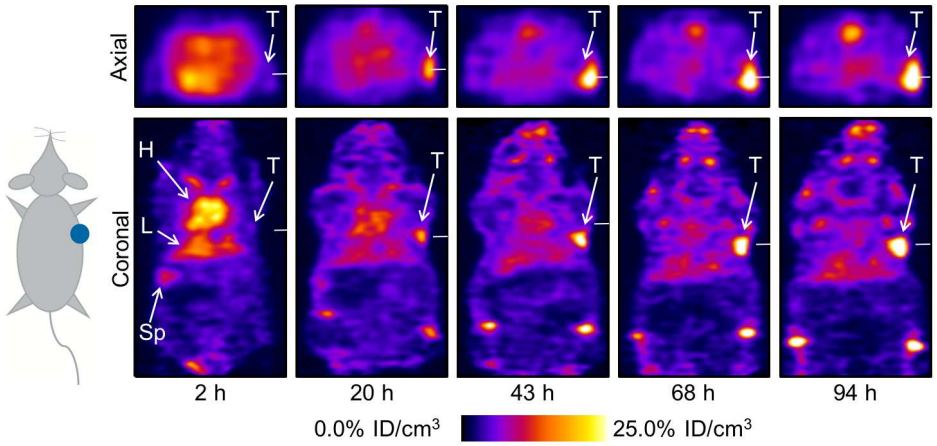

Figure S13, related to Figure 9. Temporal [^{89}Zr]ZrDFO-azepin-trastuzumab (blocking group) PET images recorded a mouse bearing SK-OV-3 tumours on the right flank. T = tumour, H = heart, L = liver, Sp = spleen.

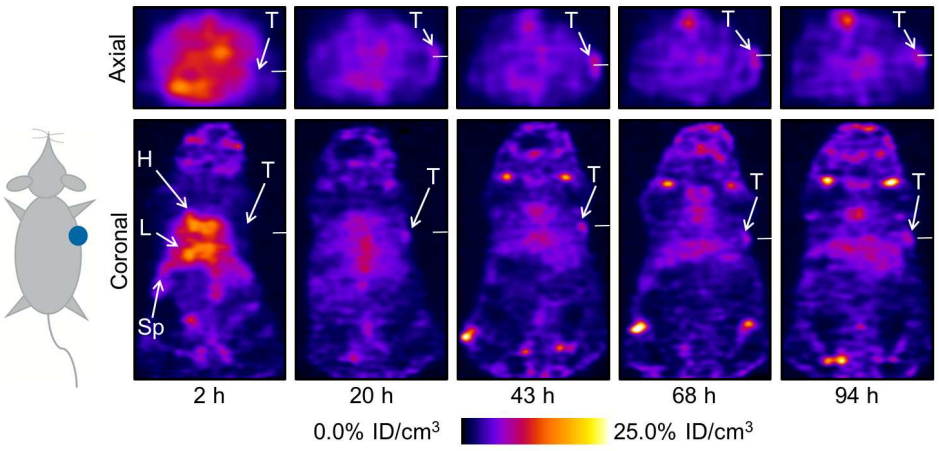

Figure S14, related to Figure 10. Time-activity bar chart showing the activity associated with different tissues (volumes-of-interest, VOI) *versus* time. Data presented are based on quantification of the PET images in units of SUV_{mean}.

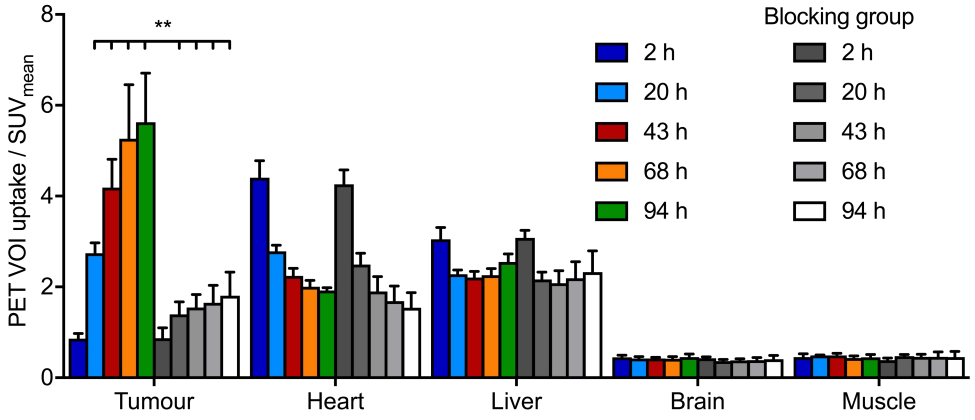

Note: Results of the Student's *t*-test analysis comparing the group of normal animals (coloured bars, $n = 5$) with the blocking group ($n = 6$) are indicated with an asterisk. (**) *P*-value < 0.01.

Measured effective half-life of [^{89}Zr]ZrDFO-azepin-trastuzumab *in vivo*

Figure S15, related to Figures 9 and 10. Plot of the measured activity retained in each mouse *versus* time.

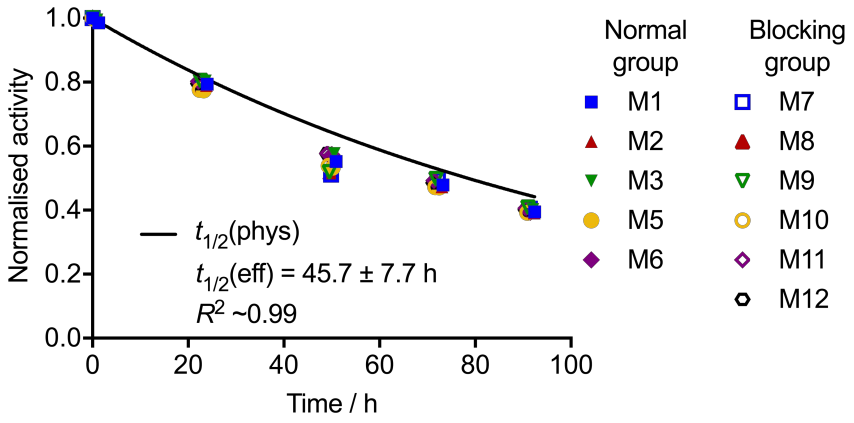

Note: mouse number 4 (M4) was excluded from the normal group.

Biodistribution data

Figure S16, related to Figure 11 and Table 1. Bar chart showing *ex vivo* biodistribution data (%ID/g) for the uptake of [^{89}Zr]ZrDFO-azepin-trastuzumab in mice bearing SK-OV-3 tumours. Data were recorded after the final imaging time point at 94 h post-injection. (***) Student's *t*-test *P*-value < 0.001.

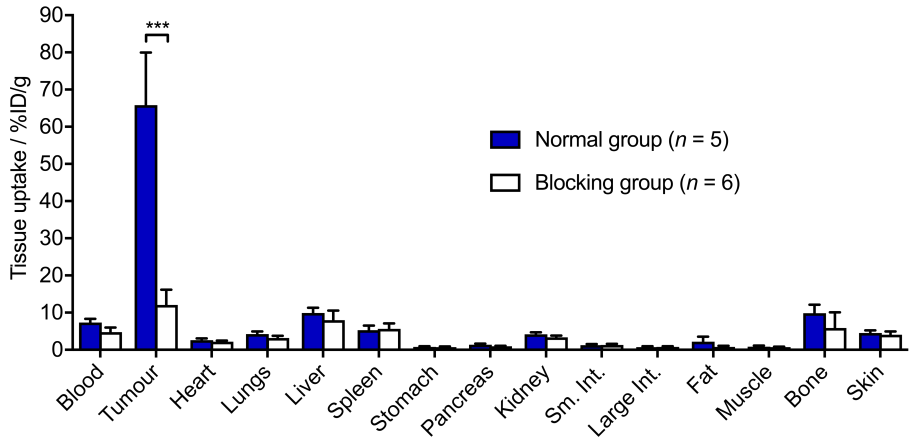

Figure S17, related to Figure 11 and Table 1. Bar chart showing *ex vivo* biodistribution data (SUV) for the uptake of [^{89}Zr]ZrDFO-azepin-trastuzumab in mice bearing SK-OV-3 tumours. Data were recorded after the final imaging time point at 94 h post-injection. (***) Student's *t*-test *P*-value < 0.001.

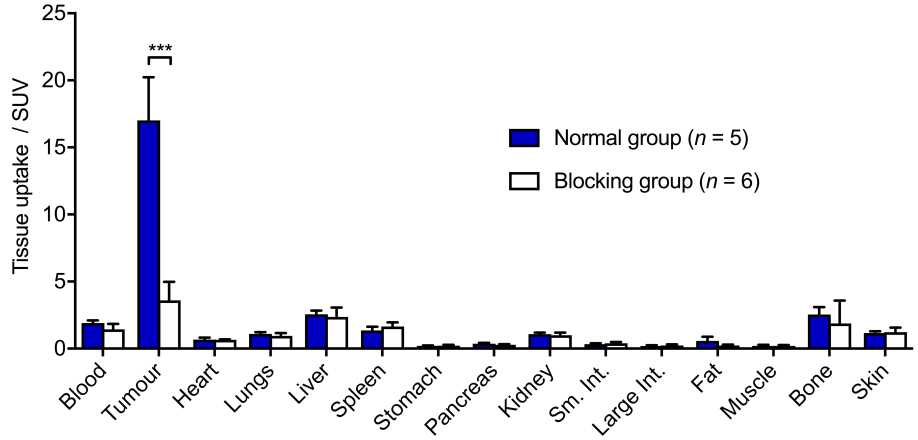

Figure S18, related to Figure 11 and Table 1. Bar chart showing tumour-to-tissue contrast ratio calculated from the *ex vivo* biodistribution data (in units of %ID/g) for the uptake of [^{89}Zr]ZrDFO-azepin-trastuzumab in mice bearing SK-OV-3 tumours.

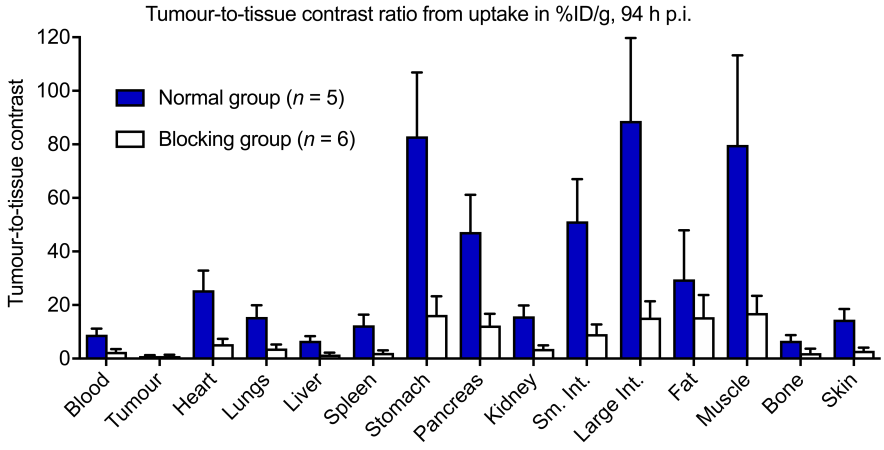

Figure S19, related to Figures 9, 10 and 11, and Table 1. Maximum intensity projection (MIP) images showing the temporal distribution of [^{89}Zr]ZrDFO-azepin-trastuzumab recorded in normal (top) and blocking (bottom) mice bearing SK-OV-3 tumours on the right flank. T = tumour, H = heart, L = liver, Sp = spleen.

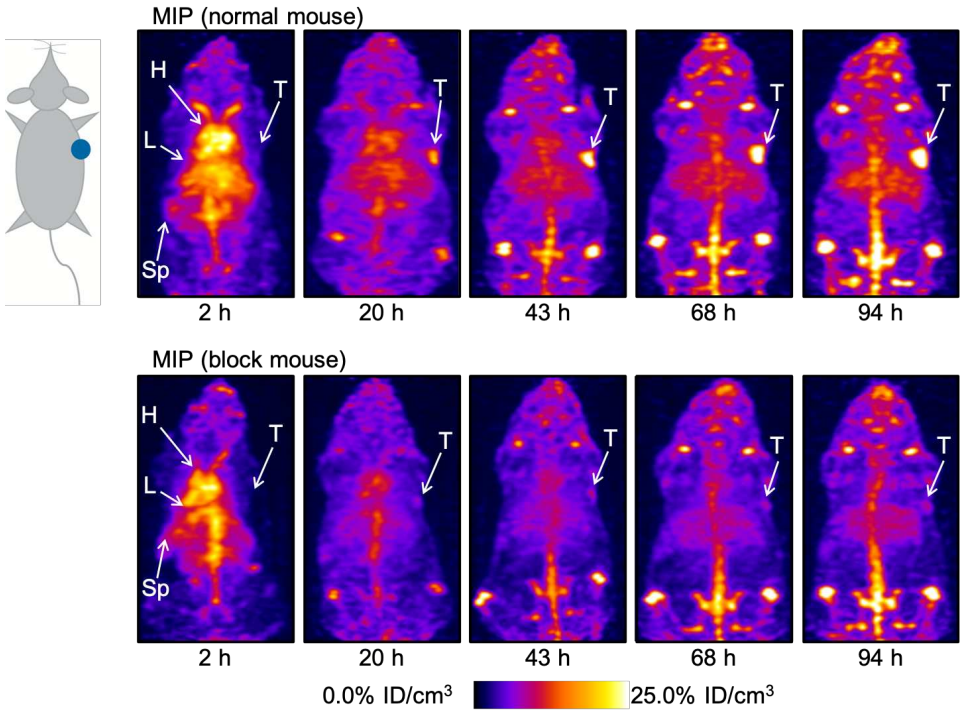

Figure S20, related to Figure 11 and Table 1. Bar chart showing a comparison between the measured tumour-to-tissue contrast ratios calculated from the *ex vivo* biodistribution data (in units of %ID/g) for the uptake of [^{89}Zr]ZrDFO-azepin-trastuzumab in mice bearing SK-OV-3 tumours, and previously reported biodistribution data on the uptake of [^{89}Zr]ZrDFO-Nsucc-trastuzumab in mice bearing BT-474 tumours.[8]

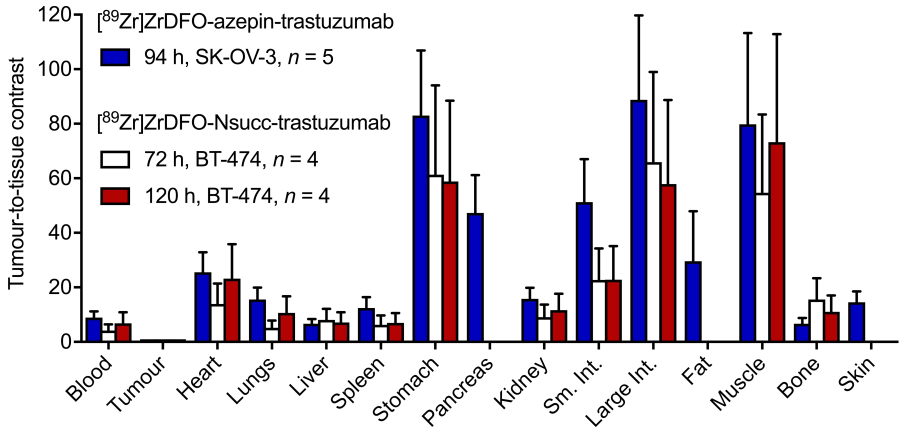

Simultaneous, one-pot photoradiochemical synthesis of [^{89}Zr]ZrDFO-azepin-trastuzumab

Simultaneous, one-pot photochemical conjugation and radiolabelling reactions were performed in accordance with the following general procedure. A stock solution of DFO-ArN_3 (**1**, 0.68 mg, 0.964 μmol) was dissolved in H_2O (50 μL) and NaOH(aq.) (30 μL of a 0.1 M stock solution). The pH of the DFO-ArN_3 solution was reduced to ~8 – 9 by the addition of HCl(aq.) (2 x 10 μL of a 0.1 M stock solution). Different reactions and control were performed at the same time using the same stock solutions. Details are given in Table S3 below. Details for reaction 1 are given here. To a transparent glass vial containing water (50 μL) was added an aliquot of pre-purified trastuzumab stock solution (stock concentration = 23.0 mg/mL, 50 μL added, 1.15 mg of protein, 7.69 nmol), an aliquot of the DFO-ArN_3 stock solution (**1**, 23 μL, 0.222 μmol, ~28.9-fold excess) and an aliquot of pre-neutralised [^{89}Zr][Zr(C_2O_4)$_4$]$^{4-}$(aq.) stock solution (50 μL, 4.2 MBq). Note: see the radiochemistry sections above for details about neutralisation of oxalic acid in the ^{89}Zr stock solution. The total reaction volume was kept constant at 150 μL for all reactions. Reactions were stirred and irradiated at room temperature for 10 min. at the specified LED wavelength (100% power). Reactions were then quenched by the addition of DTPA (10 μL, 50 mM) and aliquots of the crude reaction mixtures were analysed by using radio-ITLC, analytical PD-10-SEC and SEC-UHPLC. Data are presented in Figure 12 (main article). For reaction 1, an aliquot of the crude, quenched mixture was also purified by preparative PD-10-SEC and spin column centrifugation. After isolation of purified [^{89}Zr]ZrDFO-azepin-trastuzumab by preparative PD-10-SEC (collecting the 0.0 – 2.0 mL high molecular weight fraction using sterile PBS as an eluent) the decay corrected radiochemical yield was ~76% and the estimated lower limit (assuming no protein losses) of the molar activity was 0.41 MBq/nmol of protein. Aliquots of the purified sample of reaction 1 were then concentrated and analysed by analytical PD-10-SEC and SEC-UHPLC.

Table S3, related to Figure 12. Experimental data on the conditions used in the simultaneous photoradiolabelling reactions for the synthesis of [^{89}Zr]ZrDFO-azepin-trastuzumab.

Solution	Reaction 1	Reaction 2 (no chelate control)	Reaction 3 (no antibody control)	Reaction 4
Vol. water / μL	27	50	27	27
Vol. DFO-ArN_3 stock / μL	23	0	23	23
Vol. trastuzumab stock / μL	50	50	0	50
Vol. [^{89}Zr][Zr(C_2O_4)$_4$]$^{4-}$ stock / μL	50	50	50	50
Total volume / μL	150	150	150	150
Activity	~4.2 MBq	~4.2 MBq	~4.2 MBq	~4.2 MBq
Irradiation λ / nm	365	365	365	395
Irradiation time / min.	10	10	10	10

References

1. Srinivas, N., Jetter, P., Ueberbacher, B.J., Werneburg, M., Zerbe, K., Steinmann, J., Van Der Meijden, B., Bernardini, F., Lederer, A., Dias, R.L.A., *et al.* (2010). Peptidomimetic antibiotics target outer-membrane biogenesis in pseudomonas aeruginosa. Science (80-.). *327*, 1010–1013.
2. Zanzonico, P. (2008). Routine Quality Control of Clinical Nuclear Medicine Instrumentation: A Brief Review. J. Nucl. Med. *49*, 1114–1131.
3. Ziegler, T., and Rank, A. (1977). On the Calculation of Multiplet Energies by the Hartree-Fock-Slater Method. Theor. Chim. Acta *43*, 261–271.
4. Lindmo, T., Boven, E., Cuttitta, F., Fedorko, J., and Bunn, P.A. (1984). Determination of the immunoreactive function of radiolabeled monoclonal antibodies by linear extrapolation to binding at infinite antigen excess. J. Immunol. Methods *72*, 77–89.
5. Institute for Laboratory Animal Research (2011). Guide for the Care and Use of Laboratory Animals: 8th Ed.
6. Fridman, R., Benton, G., Aranoutova, I., Kleinman, H.K., and Bonfil, R.D. (2012). Increased initiation and growth of tumor cell lines, cancer stem cells and biopsy material in mice using basement membrane matrix protein (Cultrex or Matrigel) co-injection. Nat. Protoc. *7*, 1138–1144.
7. Bai, B., Dahlbom, M., Park, R., Hughes, L., Dagliyan, G., Yap, L.P., and Conti, P.S. (2012). Performance comparison of GENISYS4 and microPET preclinical PET scanners. IEEE Nucl. Sci. Symp. Conf. Rec. *bai*, 3765–3768.
8. Holland, J.P., Caldas-Lopes, E., Divilov, V., Longo, V. a, Taldone, T., Zatorska, D., Chiosis, G., and Lewis, J.S. (2010). Measuring the pharmacodynamic effects of a novel Hsp90 inhibitor on HER2/neu expression in mice using Zr-DFO-trastuzumab. PLoS One *5*, e8859.